Depositional age and provenance of high-grade paragneisses from the Mérida Andes, Venezuela: Implications for the Ediacaran–Cambrian tectonic setting of northwestern Gondwana

M. Daniela Tazzo-Rangel [a,*], Bodo Weber [a], Dirk Frei [b], Reneé González-Guzmán [a]

[a] *Departamento de Geología, División de Ciencias de la Tierra, Centro de Investigación Científica y de Educación Superior de Ensenada B.C. (CICESE), Carretera Ensenada-Tijuana #3918, 22860 Ensenada, BC, Mexico*
[b] *Department of Earth Sciences, University of the Western Cape, 7335 Bellville, Western Cape, South Africa*

ABSTRACT

Isotopic, geochemical, and geochronological data are provided to constrain sedimentary sources and depositional ages of high-grade paragneisses of the Iglesias Complex in the Mérida Andes (Venezuela). U-Pb geochronology of detrital zircons suggests a maximum depositional age of 540–530 Ma, whereas age spectra reveal sources from Pan-African-Brasiliano belts, the Amazon Craton, and Oaxaquia-Putumayo basement. Reworking of such Gondwanan sources is also reflected in whole-rock Nd and Hf crustal residence ages of ~2.0–1.3 Ga. Post-depositional disturbance of the U-Pb system by metamorphism during the early Paleozoic and Permo–Triassic is assessed through in-situ analysis of zircon rims and discordant analyses. Field evidence, geochemical and isotopic signatures are consistent with pelitic-psammitic and volcanic-volcaniclastic compositions for sedimentary protoliths. The former show provenances from continental intermediate sources, whereas the latter are probably sourced in an immature volcanic arc, suggesting the initiation of subduction of the Iapetus oceanic crust beneath northwestern Gondwana around 530 Ma. Sedimentary precursors were likely deposited during the latest Ediacaran–earliest Cambrian in an extensive continental shelf, fed by detritus draining from the topographic highs of the Pan-African-Brasiliano belts, across the Amazon craton and into the Iapetus Ocean. Thus, the main direction of sediment flow was opposite to the present-day transport from the Andes Cordillera by the Pacific Ocean to the Amazon fan in the Atlantic Ocean. Chemical trends in gneisses suggest fluvial sedimentary protoliths and cold-climate weathering at high latitudes. Metasedimentary rocks in the Mérida Andes show similarities with equivalent units in Peri-Gondwanan crustal fragments such as the Acatlán Complex and the Santander Massif, but no correlation with Ediacaran metasedimentary rocks of the Maya Block. Ediacaran–Cambrian fossiliferous sedimentary rocks in the Eastern Venezuela Basin and the Colombian foreland basin are possible equivalents but these units remained unmetamorphosed, as its paleoposition was far from the subduction trench during the Early Ordovician climax of the Famatinian orogeny.

1. Introduction

Lower Paleozoic rocks in Mexico, Central America, and northern South America are related to a continental arc in northwestern Gondwana, active from the late Cambrian to the Silurian, referred to as the Famatinian Orogeny (e.g., Ramos, 2018 and references therein). The crystalline basement in such regions contains ~1 Ga old inliers of deep continental crust associated with the Rodinia supercontinent assemblage (Fig. 1a), known as Oaxaquia in Mexico (e.g., Ortega-Gutiérrez et al., 2018 and references therein) and Putumayo in Colombia (e.g.,

Ibañez-Mejia, 2020 and references therein), which so far has not been unequivocally identified in the Mérida Andes in western Venezuela (Tazzo-Rangel et al., 2019; van der Lelij et al., 2016). Instead, the oldest rocks exposed in the Mérida Andes are the amphibolite facies gneisses, schists, and amphibolites of the Iglesias Complex (e.g., Burkley, 1976; Grauch, 1975). This metamorphic basement records a protracted geologic history, from the early Paleozoic Famatinian magmatic arc to the Early Triassic Pangea breakup (Tazzo-Rangel et al., 2020, 2019; van der Lelij et al., 2016).

Whereas the post-Ordovician history of the Mérida Andes crystalline
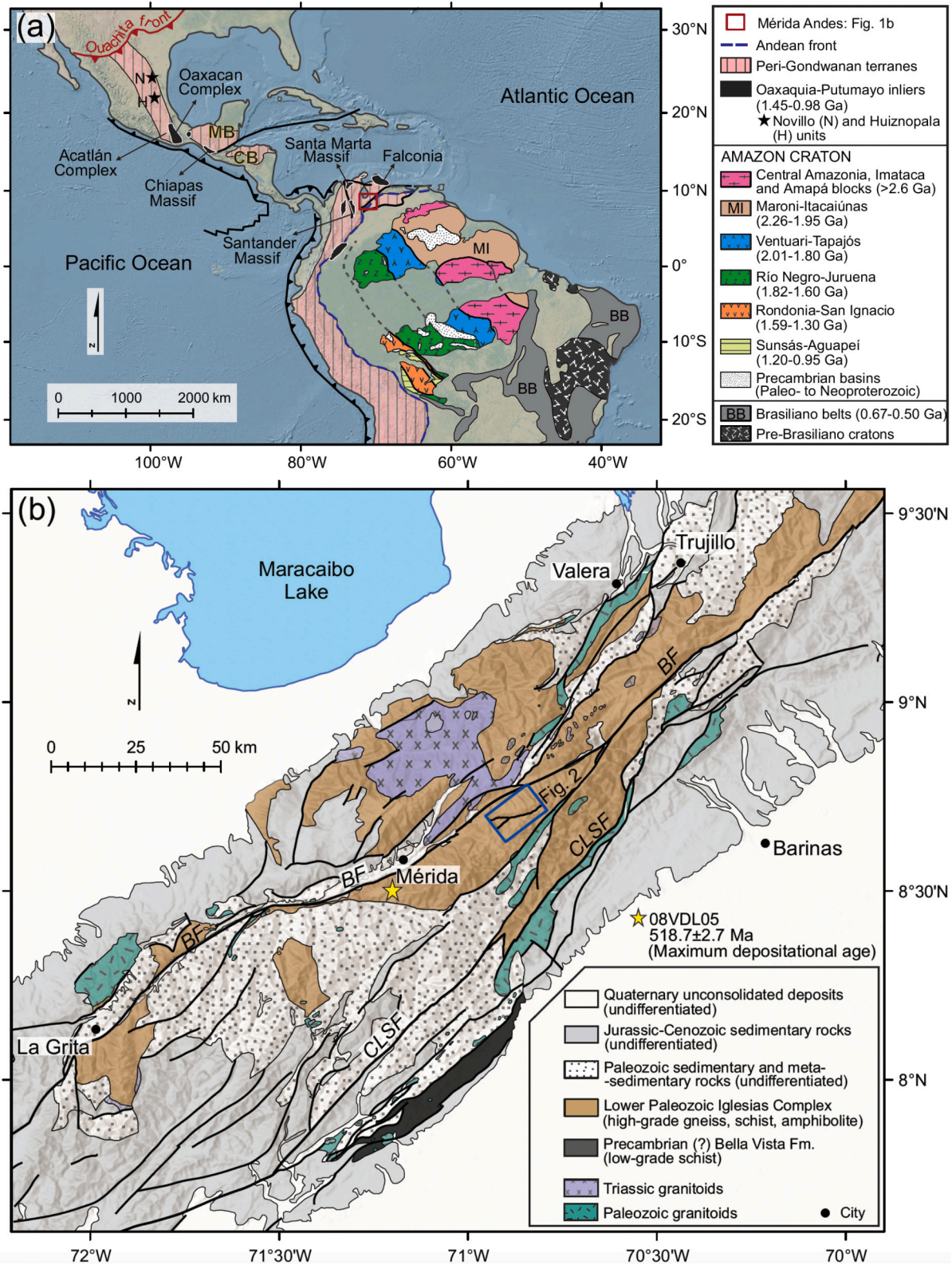
Fig. 1. (a) Location of peri-Gondwanan terranes and Rodinia-type inliers in Mexico, Central America and South America. Provinces of the Amazon Craton are also shown (modified after Ibañez-Mejia, 2020; Ibañez-Mejia and Cordani, 2020; Ramos, 2018; Weber et al., 2018). MB: Maya Block; CB: Chortís Block. (b) Simplified geologic map of the Mérida Andes in Venezuela. Adapted from van der Lelij et al. (2016). The rectangle highlights the sampling area in Fig. 2. Detrital U—Pb age (±2σ) is from van der Lelij et al. (2016). BF: Boconó Fault; CLSF: Caparo-La Soledad Fault.

basement is relatively well understood, the pre-Famatinian history remains largely unknown. Since paragneisses are apparently intruded by *syn*-kinematic early Cambrian orthogneisses (Tazzo-Rangel et al., 2019; van der Lelij et al., 2016), provenance of metasedimentary rocks may constrain the depositional age, sedimentary environment, and tectonic setting of the oldest rock-type within the Iglesias Complex.

U—Pb zircon detrital geochronology potentially provides information about source rocks and maximum depositional age estimates of sedimentary precursors, even in high-grade paragneisses (e.g., Gehrels, 2014; Gerdes and Zeh, 2006; Williams, 2001). Such information can be further improved by geochemical and isotopic data (e.g., McLennan et al., 1993; Taylor and McLennan, 1985). However, U—Pb geochronology of detrital zircon from high-grade metasedimentary rocks is commonly biased by loss of radiogenic lead and recrystallization during post-depositional metamorphism. Although the laser ablation target is the core of polished zircon grains, it is inevitable to sample recrystallized or mixed domains between the zircon core and the metamorphic rim during the ablation (e.g., Kröner et al., 2014). Therefore, Pb-loss, mixing, and discordance assessments are critical for estimating provenance and maximum depositional ages (MDA) in high-grade paragneisses (e.g., Andersen et al., 2019; Gehrels, 2014; Reimink et al., 2016; Spencer et al., 2016).

In this work, we report LA-ICP-MS U—Pb detrital zircon data of paragneisses from the Iglesias Complex in the Central Mérida Andes, evaluating the effect of recrystallized domains and metamorphic rims on estimations of depositional ages in high-grade metasedimentary rocks. Provenance is also constrained from whole-rock geochemistry and Nd—Hf isotope systematics. Our results are compared to similar peri-Gondwanan crustal fragments close to the Mérida Andes during the Paleozoic and suggest the existence of a continental shelf in the latest Ediacaran–earliest Cambrian in northwestern Gondwana, as well as the initiation of subduction of the Iapetus oceanic crust around 530 Ma.

2. The Iglesias Complex: a record of the Famatinian magmatic arc and Permo-Triassic Pangea breakup

The oldest rocks exposed in the Mérida Andes are the paragneisses, metasedimentary schists, orthogneisses, and amphibolites of the Iglesias Complex (e.g., Burkley, 1976; Grauch, 1975) (Fig. 1b). Magmatic protoliths of orthogneisses and amphibolite dikes intruding paragneisses yield zircon U—Pb ages between 487.2 ± 7.0 Ma and 458.0 ± 3.4 Ma, whereas in-situ LA-ICP-MS U—Pb data from solid-state recrystallization and anatectic overgrowths in zircons reveal multiple metamorphic events at ca. 470 Ma, ca. 450 Ma, and ca. 420 Ma (Tazzo-Rangel et al., 2019). Such tectonothermal events are related to alternating phases of compression and extension in the Famatinian magmatic arc, formed by subduction of the Iapetus oceanic crust underneath western Gondwana (e.g., Ramos, 2018; Tazzo-Rangel et al., 2019; van der Lelij et al., 2016). The amphibolite-facies basement was intruded by numerous granitoid plutons in two magmatic cycles: during the Cambrian–Silurian, contemporaneous with the Famatinian Orogeny, and during the Triassic (ca. 247–213 Ma), suggesting a magmatic hiatus from ca. 414 Ma to ca. 250 Ma (van der Lelij et al., 2016).

The Iglesias Complex is overlain by Paleozoic sedimentary and metasedimentary units, Jurassic volcano-sedimentary sequences, and Cretaceous–Paleocene sedimentary rocks (González de Juana et al., 1980) (Fig. 1b). The Bella Vista Formation is probably a low-grade metamorphic equivalent of the Iglesias Complex, but it is restricted to a ~10 km wide belt to the south in the Caparo region (Burkley, 1976; González de Juana et al., 1980). Greenschist-facies metapelitic rocks of the Bella Vista Formation are unconformably overlain by Ordovician–Silurian unmetamorphosed sedimentary rocks (e.g., Burkley, 1976; González de Juana et al., 1980).

Recent U—Pb secondary ion mass spectrometry data on unpolished zircon surfaces and garnet Sm—Nd dating disclose the latest Permian–earliest Triassic metamorphism in the Iglesias Complex at 251 ± 4

Ma, possibly driven by post-orogenic gravitational collapse after the collision of Gondwana and Laurentia to form Pangea (Tazzo-Rangel et al., 2020). Geothermobarometry and Rb—Sr thermochronology of mica suggest upper amphibolite-facies peak conditions, followed by cooling and retrogression during the Triassic–Early Jurassic as a consequence of thermal relaxation and onset of extension during Pangea breakup (Tazzo-Rangel et al., 2020).

The Paleozoic–early Mesozoic magmatic and metamorphic history of the Iglesias Complex has several similarities to rocks of the same age in other crustal fragments adjacent to northwestern Gondwana, such as the Santander Massif and the Sierra Nevada de Santa Marta in Colombia, as well as the Acatlán Complex and the Maya Block in southern Mexico-Central America (Fig. 1a; e.g., González-Guzmán et al., 2016a; Ramos, 2018; Tazzo-Rangel et al., 2019; van der Lelij et al., 2016; Weber et al., 2018).

3. Metasedimentary rocks in the Iglesias Complex

Paragneisses and metasedimentary schists are divided into two groups according to protolith composition: metapelitic-metapsammitic and metavolcanic or metavolcaniclastic rocks. Both rock types display an inequigranular coarse- to finely-crystalline texture and schistose to gneissic fabrics. Small outcrops of hornblende orthogneiss occur alternating with metasedimentary rocks, displaying a coarse-grained equigranular texture and hosting plagioclase with low-frequency oscillatory zoning (Fig. 2; sample LMch-02 in Table 1). Mafic igneous protoliths of amphibolite lenses within para- and orthogneiss probably intruded before deformation and metamorphism (Tazzo-Rangel et al., 2019).

Partial melting during high-grade Ordovician–Silurian metamorphic events resulted in schlieren as well as layered, net, raft, and vein-like migmatite textures (e.g., Sawyer, 2008). Leucosomes are typically millimetric to centimetric (Fig. 3a) in thickness, and composed of quartz, plagioclase, and microcline, reflecting a granodioritic-granitic composition. Leucosomes display similar compositions in both pelitic and hornblende-bearing paragneiss, suggesting partial melting of the micaceous gneisses and melt injection into the volcanic or volcaniclastic layers of the sequence. Breakdown of hornblende and melting of andesitic protoliths is unlikely because such reactions would require temperatures above ~780–800 °C, even by adding an external fluid phase (e.g., Aranovich et al., 2014). Petrographic observations are not consistent with granulite facies conditions in the metamorphic basement of the Mérida Andes (Tazzo-Rangel et al., 2019).

3.1. Pelitic-psammitic metasedimentary rocks

The mineral assemblage in the pelitic-psammitic gneisses and schists is quartz + plagioclase + biotite ± garnet ± white mica ± sillimanite ± K-feldspar (Fig. 3b). Mica flakes define the penetrative foliation; sillimanite is typically prismatic or fibrous and included within biotite or white mica. In some pelitic gneisses, fibrous sillimanite forms lenticular aggregates (Fig. 3c) probably formed by the reaction quartz + muscovite = K-feldspar + sillimanite + H_2O. Garnet porphyroblasts are subhedral and poikiloblastic, hosting inclusions of biotite, quartz, feldspar, zircon, and ilmenite. Psammitic paragneisses display ~3–5 mm sized plagioclase porphyroblasts with K-feldspar lamellae exsolutions (Fig. 3d), possibly reflecting relict lithic clasts of the greywacke-like protolith. Typical accessory phases are apatite, zircon, epidote, tourmaline, and Fe—Ti oxides. The formation of secondary epidote-allanite as well as chloritization of biotite and garnet suggests greenschist-facies retrogression.

3.2. Volcanic and volcaniclastic metasedimentary rocks

Occasionally exposed hornblende-plagioclase bearing paragneisses and schists (Fig. 2) with thicknesses of no more than a few meters are interpreted as volcaniclastic or volcanic protoliths. Fifty cm to one-
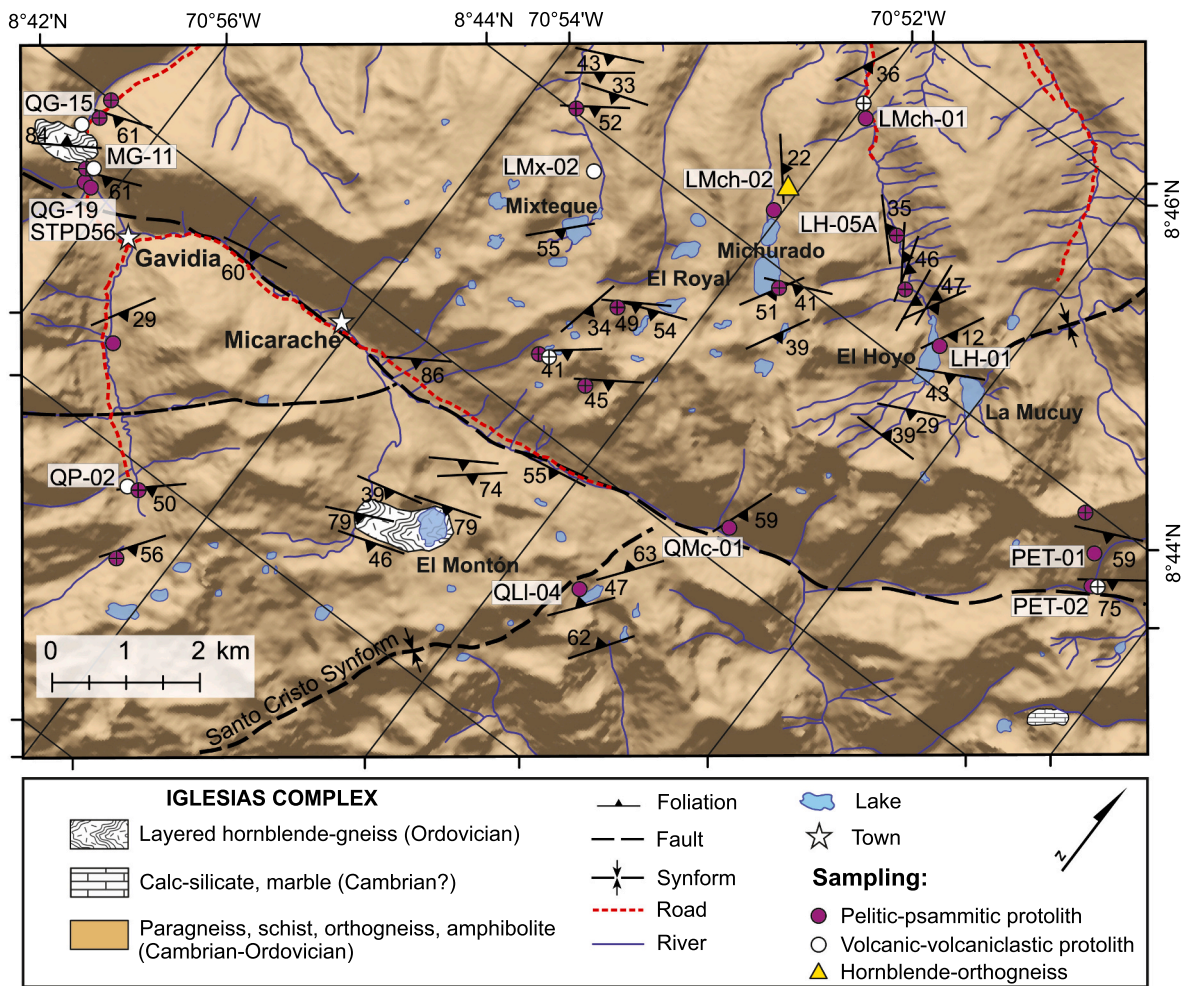
Fig. 2. Geologic map and sampling sites of the Iglesias Complex in the Central Mérida Andes (modified from Grauch, 1975). Labeled rock samples are those processed for U—Pb geochronology as well as whole-rock isotopic and chemical analyses, according to Table 1. Unlabeled samples, marked with a cross, were analyzed in thin sections only. Background digital elevation model is based on Sentinel-2 synthetic aperture radar (SAR) data processed by the European Space Agency (ESA).

meter thick grayish-greenish layers that are intercalated with metapelitic-metapsammitic rocks represent either former subvolcanic sills or lava flows (Fig. 3e). Relatively cyclic gradations between hornblende-biotite gneiss, hornblende-gneiss, and para-amphibolite within the outcrop and thin section scale probably indicate reworking of andesitic-basaltic material, mixed or intercalated with continental siliciclastic sediments (Fig. 3f), producing these volcaniclastic protoliths. The typical mineralogical assemblage is plagioclase + hornblende + biotite + quartz ± epidote ± garnet ± microcline ± titanite ± Fe—Ti oxides ± secondary actinolite. The rare ~2–3 mm garnet porphyroblasts are xenomorphic and skeletal (Fig. 3g,h). Plagioclase porphyroblasts of ~2.5 mm host inclusions of rounded quartz. In some thin sections, plagioclase displays relict concentric oscillatory zoning, indicating an igneous origin.

4. Analytical techniques

A brief description and the analyses performed in different metasedimentary rock samples of the Iglesias Complex are indicated in Table 1. Sample location is shown on the map of Fig. 2. After removing weathered portions, rock samples were crushed in a hydraulic press. A representative aliquot of the crushed rock was pulverized in a tungsten carbide mill bowl for whole-rock geochemistry and isotope analyses.

4.1. Zircon U—Pb geochronology

Zircon crystals from six rock samples were separated at Departamento de Geología, Centro de Investigación Científica y de Educación Superior de Ensenada, Baja California (CICESE), Mexico, using standard density and magnetic techniques: Wilfley table, Frantz magnetic separator, and heavy liquids (Sodium Polytungstate). Grains were mounted randomly (e.g., Gehrels, 2014) in epoxy mounts and polished to expose cores. The polished mounts were coated with carbon and imaged with cathodoluminescence (CL) with a Jeol JSM35C scanning electron microscope at CICESE, before and after the U—Pb analyses.

U—Pb geochronology on detrital zircon grains was performed by laser ablation inductively coupled plasma mass spectrometry (LA-ICP-MS) at the Central Analytical Facilities (CAF), Stellenbosch University, South Africa. A Thermo Element2 mass spectrometer coupled to a NewWave UP213 laser ablation system ($\lambda = 213$ nm, f = 10 Hz, fluency = 3.5 J/cm^{-2}) was used, following methods for analysis and data processing described in detail by Gerdes and Zeh (2006) and Frei and Gerdes (2009). U—Pb data were obtained from ablation spots of 30 μm. GJ-1 reference zircon was used as a primary standard (608.5 ± 0.4 Ma, Jackson et al., 2004). Measurements were verified using fragments of Plešovice (337.1 ± 0.4 Ma; Sláma et al., 2008), 91500 (1065.4 ± 0.3 Ma; Wiedenbeck et al., 1995), Temora 1 (416.8 ± 1.1 Ma; Black et al., 2003), and M127 (524.4 ± 0.2 Ma; Nasdala et al., 2016) zircon standards, yielding Concordia ages of 337.8 ± 1.1 Ma (2σ, n = 37, MSWD = 0.47),

Table 1
Classification, location, and brief description of rock samples of the Iglesias Complex analyzed in this study.

Sample	Rock type	Lat (N)	Long (W)	Brief description[a]	U-Pb (LA-ICPMS)	Whole-rock geochemistry	Sm-Nd isotopes	Lu-Hf isotopes
					Analysis			
PET-01	Pelitic-psammitic paragneiss	8° 43′ 47″	70° 48′ 39″	Qtz + Pl + Bt + Grt + Wm + Sil + Kfs. Schistosity is defined by biotite.	✔	✔	✔	
QLl-04		8° 41′ 16″	70° 51′ 26″	Qtz + Bt + Wm. Penetrative foliation defined by mica.	✔	✔	✔	
LMch-01		8° 45′ 17″	70° 51′ 52″	Qtz + Pl + Bt + Kfs + Wm + Sil + Czo. Chessboard Qtz, myrmekite texture, and flame perthite in Kfs.	✔			
QG-19		8° 41′ 26″	70° 56′ 9″	Qtz + Pl + Bt + Sil + Kfs + Wm. Wm reacts to form Kfs + Sil.	✔			
LH-05A		8° 45′ 35″	70° 52′ 14″	Qtz + Pl + Bt + Grt. Garnet porhyroblasts (ca. 5 mm) are *syn-* to post-kinematic	✔	✔	✔	✔
QMc-01		8° 42′ 16″	70° 50′ 54″	Bt + Qtz + Sil + Ms. + Pl. Fibrous Sil in lenticular aggregates.		✔	✔	✔
LH-01		8° 44′ 15″	70° 50′ 27″	Qtz + Pl + Bt + Wm + Sil. Sillimanite nodules of ~5 mm.		✔	✔	
PET-02		8° 43′ 34″	70° 48′ 30″	Qtz + Bt + Pl + Sil + Wm. Bt partially retrogressed to chlorite and white mica.		✔	✔	✔
STPD-56[b]		8° 41′ 26″	70° 56′ 9″	Qtz + Bt + Pl + Mc. Meso-perthitic texture in ~5 mm blasts. Epidote and chlorite as retrogression phases.	✔	✔	✔	✔
QG-15	Volcanic-volcaniclastic paragneiss	8° 41′ 41″	70° 56′ 24″	Hbl + Pl + Bt + Qtz + Opq. Gradations between Bt-rich and Hbl-rich layers.	✔	✔	✔	✔
MG-11		8° 41′ 26″	70° 56′ 8″	Pl + Qtz + Bt + Hbl + Opq. Gradations between Bt-rich and Hbl-rich layers. Retrogressional epidote-allanite.		✔	✔	✔
QP-02		8° 39′ 45″	70° 54′ 32″	Pl + Hbl + Bt + Qtz + Grt ± Act. Grt is xenomorphic and skeletal. Actinolite is secondary.		✔	✔	✔
LMx-02		8° 43′ 44″	70° 53′ 15″	Qtz + Pl + Hbl + Bt + Grt. Slightly zoned Pl. Epidote and chlorite as retrogression phases.		✔	✔	✔
LMch-02	Hornblende-orthogneiss	8° 44′ 31″	70° 52′ 4″	Pl + Hbl + Qtz + Bt + Opq. Low-frequency oscillatory zoning in Pl.	✔	✔	✔	✔

[a] Mineral abbreviations after Whitney and Evans (2010). Act: Actinolite, Bt: Biotite, Czo: Clinozoisite, Grt: Garnet, Hbl: Hornblende, Kfs: K-feldspar; Mc: Microcline, Opq: Opaque mineral, Pl: Plagioclase, Qtz: Quartz, Sil: Sillimanite. Wm: White mica.
[b] Data from Tazzo-Rangel et al. (2019).

1065.4 ± 3.2 Ma (2σ, $n = 53$, MSWD = 0.81), 416.3 ± 4.1 Ma (2σ, $n = 7$, MSWD = 0.31), and 530.6 ± 7.3 Ma (2σ, $n = 4$, MSWD = 0.27), respectively.

The LA-ICPMS analysis of zircons from sample QG-15 was at the Peter Hooper GeoAnalytical Lab facilities of the Washington State University (Pullman, WA). Measurement details are specified in Tazzo-Rangel et al. (2019).

U—Pb analyses are shown on Wetherill Concordia diagrams plotted on IsoplotR (Vermeesch, 2018), using 2σ error ellipses. Apparent ages in Kernel Density Estimation diagrams (KDE) are $^{206}Pb/^{238}U$ for grains <0.8 Ga and $^{207}Pb/^{206}Pb$ for grains ≥0.8 Ga (e.g., Gehrels et al., 2008). Concordia and intercept ages are reported with an uncertainty of ±2σ. KDE diagrams were plotted with a bandwidth of 20 Ma (e.g., Spencer, 2020) whereas the binwidth in histograms is 25 Ma.

4.2. Whole-rock geochemistry

Chemical analyses of rock powders were carried out commercially at Activation Laboratories Ltd. (Ontario, Canada), under the 4LithoRes package. Fused samples are diluted in Li-tetraborate flux and analyzed by Inductively Coupled Plasma-Optical Emission Spectroscopy (ICP-OES) for major elements and by ICP-MS for trace elements. A set of certified reference materials and two duplicated unknown samples were run in the same batch. At a 95% confidence level, the relative uncertainties in the measurement of major and trace elements are ≤3% and ≤ 10%, respectively. Detailed procedures for sample preparation and measurements are specified at https://actlabs.com/

4.3. Sm—Nd and Lu—Hf isotope systematics

Sample preparation and element separation for Sm—Nd and Lu—Hf isotope analyses of rock powders were carried out in PicoTrace clean lab facilities at Departamento de Geología, CICESE, after procedures described in detail elsewhere (González-Guzmán et al., 2016a, 2016b; Weber et al., 2018).

Measurements of Lu and Hf isotopes in solutions were accomplished in a Thermo NeptunePlus multi-collector ICP-MS at the Laboratorio de Estudios Isotópicos (LEI) of UNAM (Querétaro, Mexico) after protocols of González-Guzmán et al. (2016b). Samarium and Nd isotopes were analyzed by thermal ionization mass spectrometry (TIMS) using a Thermo TritonPlus equipment installed at the Laboratorio Universitario de Geoquímica Isotópica (LUGIS) of UNAM, Mexico City, according to procedures of González-Guzmán et al. (2016a) and Weber et al. (2018). Six rock samples (LH-01, QLl-04, PET-01, QMc-01, LH-05A, PET-02) were analyzed with a Nu-Instruments TIMS at Departamento de Geología, CICESE, with procedures described in detail in Tazzo-Rangel et al. (2020). Lu—Hf data reduction was performed offline using the IsotopeHf® program written in R software (González-Guzmán et al., 2016b). In-house Excel spreadsheets were used for reduction and correction of Sm—Nd data. Mass bias correction for Sm, Nd, and Hf, was achieved by normalizing to one accepted constant isotopic ratio using the exponential law (Sm: $^{152}Sm/^{147}Sm = 1.7845352$; Nd: $^{146}Nd/^{144}Nd = 0.7219$; $^{179}Hf/^{177}Hf$ of 0.7325). Lutetium mass bias correction was performed by doping the solution sample with Re and using the trend defined by an external standard of known isotopic composition of Lu +
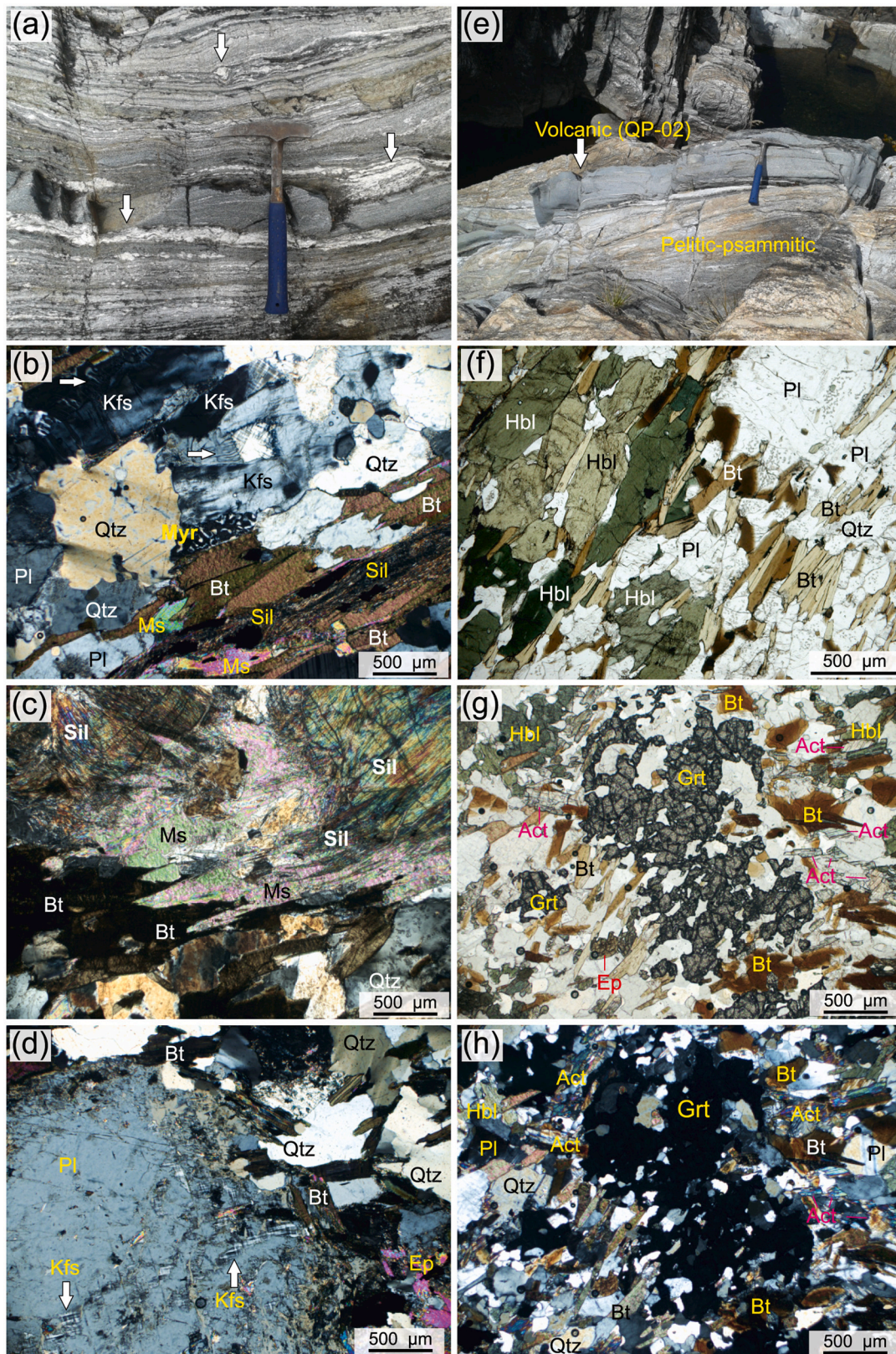
Fig. 3. (a) Stromatic and nebulitic textures (arrows) in migmatized pelitic-psammitic gneiss. (b) Typical mineralogical assemblage in pelitic gneiss (sample LMch-01): Qtz + Pl + Kfs + Bt + Ms. + Sil. Flame perthite is observed in Kfs (arrows); Myr: Myrmekite texture. (c) Muscovite breakdown to form sillimanite nodules in pelitic schist (sample QMc-01). (d) Antiperthite texture in relict plagioclase porphyroblasts in greywacke-like gneiss. Epidote is a secondary phase. (e) Layer of greenish hornblende-bearing gneiss, probably a basaltic sill protolith, in pelitic-psammitic gneiss. (f) Hornblende-rich and biotite-rich layer gradation in volcani-clastic gneiss. (g-h) Typical mineralogical assemblage in the basaltic protolith layer shown in (b): Pl + Hbl + Bt + Qtz + Ep + Grt ± (secondary) Act (sample QP-02). Thin section microphotographs in crossed polarized light, except (f) and (g). Mineral abbreviations after Whitney and Evans (2010) (see Table 1).

Re that is measured interspersed with samples during the run sessions (González-Guzmán et al., 2016b). Typical external reproducibilities are 0.003% for both ^{176}Hf/^{177}Hf and ^{143}Nd/^{144}Nd, 0.5% for parent/daughter ratios (^{176}Lu/^{177}Hf and ^{147}Sm/^{144}Nd), and 2% for element concentrations (Weber et al., 2018).

5. Results

5.1. U—Pb detrital zircon geochronology

Geochronology results of paragneiss analyzed in this study are summarized in Table 2, whereas the full dataset is listed in the Supplementary Table 1. Specific zircon U—Pb ages discussed in this work are Concordia ages. Several sophisticated methods have been proposed to approach discordance of detrital zircons (e.g., Reimink et al., 2016 and references therein). In this work, we used one of the most common methods to filter discordant data, by excluding analyses that plot outside an envelope around the Concordia curve defined by 10% discordance (e. g., Andersen et al., 2019 and references therein). However, age spectra diagrams are plotted using filtered and unfiltered data to provide robust interpretation of zircon populations (e.g., Gehrels, 2014; Spencer et al., 2016).

Zircon grains from paragneisses of the Iglesias Complex are rounded to bipyramidal. CL images of internal structures reveal homogeneous to oscillatory zoning patterns in darkish- to bright-CL cores and well-defined rims (Fig. 4 and Fig. 5). Some cores display recrystallization fronts (e.g., Rubatto, 2017 and references therein). Distinct CL responses in rims highlight different growth/recrystallization domains, possibly related to multiple metamorphic events during the Ordovician–Silurian and the Permo–Triassic (Tazzo-Rangel et al., 2020, 2019). In contrast, zircons from the hornblende-orthogneiss sample LMch-02 have cores and rims with sector and oscillatory zoning (Fig. 6).

Samples PET-01, QLl-04, and LMch-01 (Fig. 4) yielded mostly concordant analyses in zircon cores, with ages ranging from ca. 2.7 Ga to 506 Ma. However, complex zircon core recrystallization is evident in the U—Pb systematics, given that between 8% and 15% of analyses are discordant, possibly reflecting Pb loss of Meso- and Paleoproterozoic zircons during the Triassic and the Silurian, as calculated from Discordia lines. Th/U ratios in concordant zircon cores are mostly above 0.1, suggesting that metamorphic recrystallization/growth is not significant (e.g., Rubatto, 2017 and references therein). Mixed core-rim domains in

zircons from sample LMch-01 yielded ages between ca. 471 and 240 Ma.

As a proxy for identifying the age of metamorphism in the analyzed high-grade paragneisses (e.g., Zimmermann et al., 2018), we measured metamorphic rims in samples QG-19 and LH-05A. Such measurements are also useful to evaluate the effect of metamorphism in complexly zoned zircons when trying to establish maximum depositional ages (MDA) of sedimentary protoliths from the youngest detrital domains. For this purpose, it is crucial to distinguish between the youngest detrital and the oldest metamorphic domains. Almost all concordant U—Pb analyses in zircon rims yielded ages of ca. 489–245 Ma, and only five out of 75 analyses have Th/U > 0.1 (Fig. 5a,b). Mixed and reset domains have ages ranging from ca. 399 Ma to 283 Ma all with Th/U ratios lower than 0.1. Concordant ages between ca. 2.2 Ga and 546 Ma were obtained in zircon cores.

Basaltic-andesitic sill- or lava-like protoliths form zircon-poor, mafic gneisses. Sample QP-02 (Fig. 3e) was processed twice for zircon separation, yielding insufficient zircon grains for representative analyses. Thirty-nine concordant analyses measured on rounded and small zircons in volcaniclastic gneiss QG-15 yielded U—Pb ages ranging from ca. 694 Ma to 451 Ma, as well as a few zircons around ca. 2.4 Ga, 1.8 Ga, and 1.1 Ga (Fig. 5c). U—Pb ages of 460–450 Ma are probably related to anatexis, and may be analogous to metamorphic or magmatic zircons from hornblende orthogneisses in the Mérida Andes basement (Tazzo-Rangel et al., 2019).
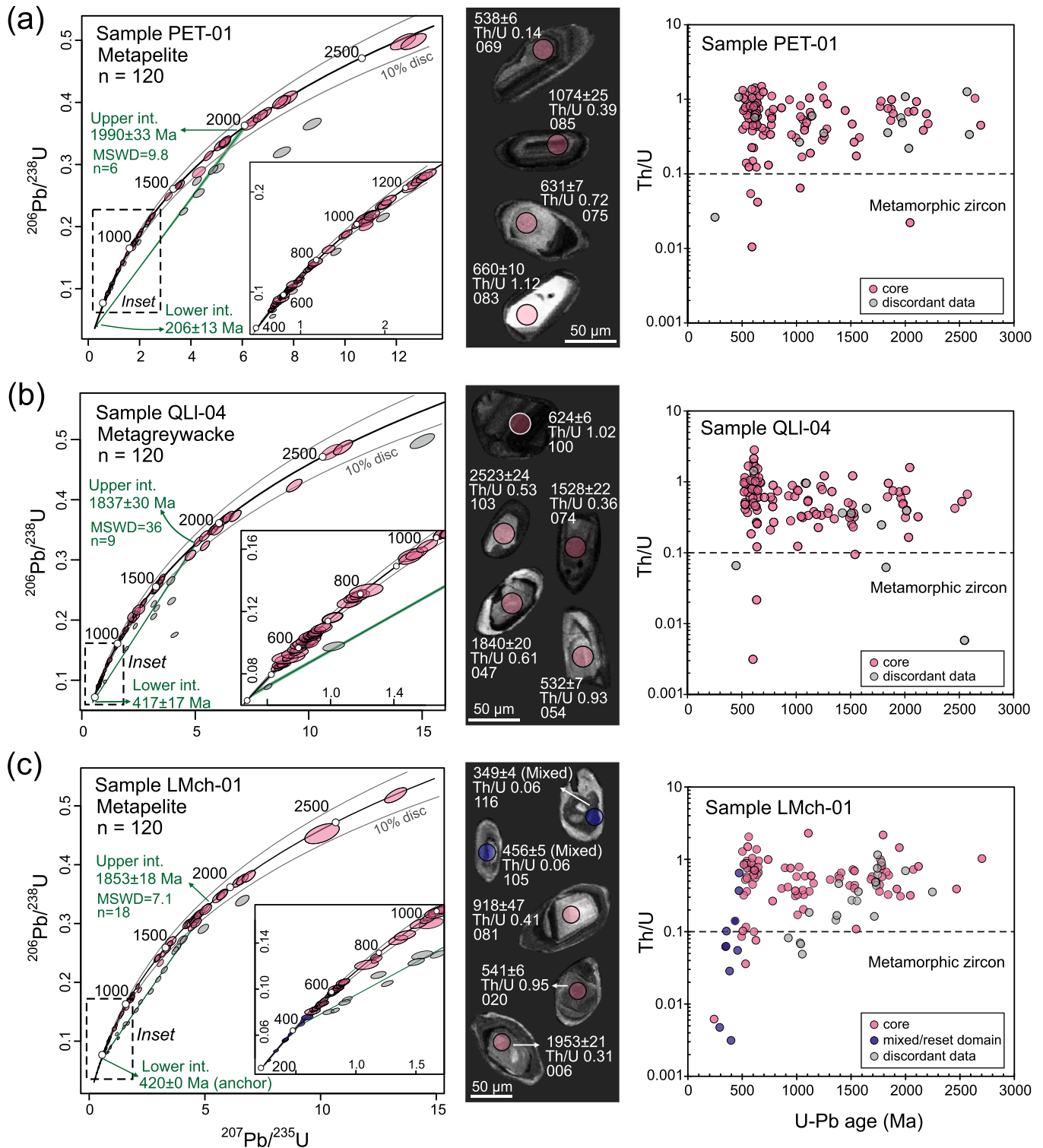
Sample LMch-02 corresponds to a hornblende-biotite equigranular orthogneiss, intercalated within a paragneiss with greywacke compositions. Well-developed oscillatory zoning in CL images suggests that zircon precipitated from magmatic melts. U—Pb ages of rim and core domains overlap in the range of 481–410 Ma, whereas mixed domains have younger ages ranging from ca. 402 to 296 Ma (Fig. 6). Only one core in sample LMch-02 has an age of 948 ± 34 Ma (2σ; not shown). Although the measured ages in zircon rims of paragneisses are quite similar to those in the orthogneiss sample, all analyses in the latter (except one) have Th/U > 0.1, suggesting different chemical signatures and, therefore, a distinct formation mechanism. An upper intercept age of 478 ± 14 Ma implies that Early Ordovician magmas intruded the sedimentary protoliths (Fig. 6).

In Fig. 7, we report the composite detrital-zircon KDEs for paragneisses of the Iglesias Complex, considering all U—Pb analyses and filtered data in the detrital fraction, that is, excluding analyses <10% discordant and metamorphic rims or mixed domains. Samples PET-01, QLl-04, and LMch-01 display very similar age spectra with significant age modes at ca. 630 Ma and 530 Ma, as well as less pronounced modes around 1870–1770 Ma, 1520 Ma, and 1050–1000 Ma. Samples QG-19 and LH-05A have prominent modes at ca. 420 Ma and 415 Ma that correspond with unfiltered data of metamorphic rims and mixed domains. Such modes in the age spectra are practically inexistent when considering detrital cores only. Age modes in the volcaniclastic gneiss QG-15 (Fig. 7h) are near 610 Ma, 525 Ma, and 460 Ma.

For comparison, detrital zircon data of the Iglesias Complex reported by van der Lelij et al. (2016) and Tazzo-Rangel et al. (2019) are also shown in KDEs of Fig. 7. A few detrital cores in sample STPD-56 (Fig. 7f) form a meaningful age mode around 1040 Ma, although measurements were performed mostly in metamorphic rims of ca. 410 Ma. Age distribution in micaceous gneiss analyzed by van der Lelij et al. (2016) is virtually identical to our samples (Fig. 7g).

The multidimensional scaling plot (MDS; Vermeesch, 2013; Fig. 7i) shows that detrital zircon U—Pb data from most paragneiss samples cluster together, suggesting an equivalent age distribution. Exceptions are those samples with (1) a relatively small number of U—Pb analyses (n < 50) and (2) a significant number of U—Pb ages measured in metamorphic rims and recrystallized domains. It is noteworthy that the orthogneiss sample LMch-02 is a nearest neighbor to the volcaniclastic gneiss QG-15.

The overall range of zircon ages in the different samples is broadly similar, containing a significant proportion of grains with ages between

Table 2
Maximum depositional ages (MDAs) for metasedimentary rocks of the Iglesias Complex.

Sample	Youngest (detrital core) graphical peak (YPP)[a]	Weighted average of the youngest grain cluster at 2σ (YGC2σ)[a,c]	τ ages (weighted average of all dates in the YPP)[b,c]
PET-01	ca. 530 Ma	528 ± 8 Ma (n = 4; MSWD = 0.29; p = 0.84)	529 ± 7 Ma (n = 5; MSWD = 0.40; p = 0.81)
QLl-04	ca. 532 Ma	528 ± 9 Ma (n = 4; MSWD = 0.01; p = 1.00)	532 ± 9 Ma (n = 4; MSWD = 0.19; p = 0.91)
LMch-01	ca. 533 Ma	518 ± 8 Ma (n = 4; MSWD = 1.79; p = 0.15)	537 ± 7 Ma (n = 5; MSWD = 0.40; p = 0.81)
QG-19	ca. 577 Ma	566 ± 18 Ma (n = 3; MSWD = 0.66; p = 0.52)	581 ± 11 Ma (n = 4; MSWD = 5.8; p = 0.001)
QG-15	ca. 525 Ma	507 ± 38 Ma (n = 3; MSWD = 0.17; p = 0.84)	527 ± 30 Ma (n = 4; MSWD = 0.24; p = 0.87)

[a] Dickinson and Gehrels (2009).
[b] Barbeau et al. (2009).
[c] Uncertainty in ages is 95% conf. level. n = number of single detrital grains. MSWD = Mean Square of the Weighted Deviates for age homogeneity. p = Chi-squared p-value for the age homogeneity test (Vermeesch, 2018).
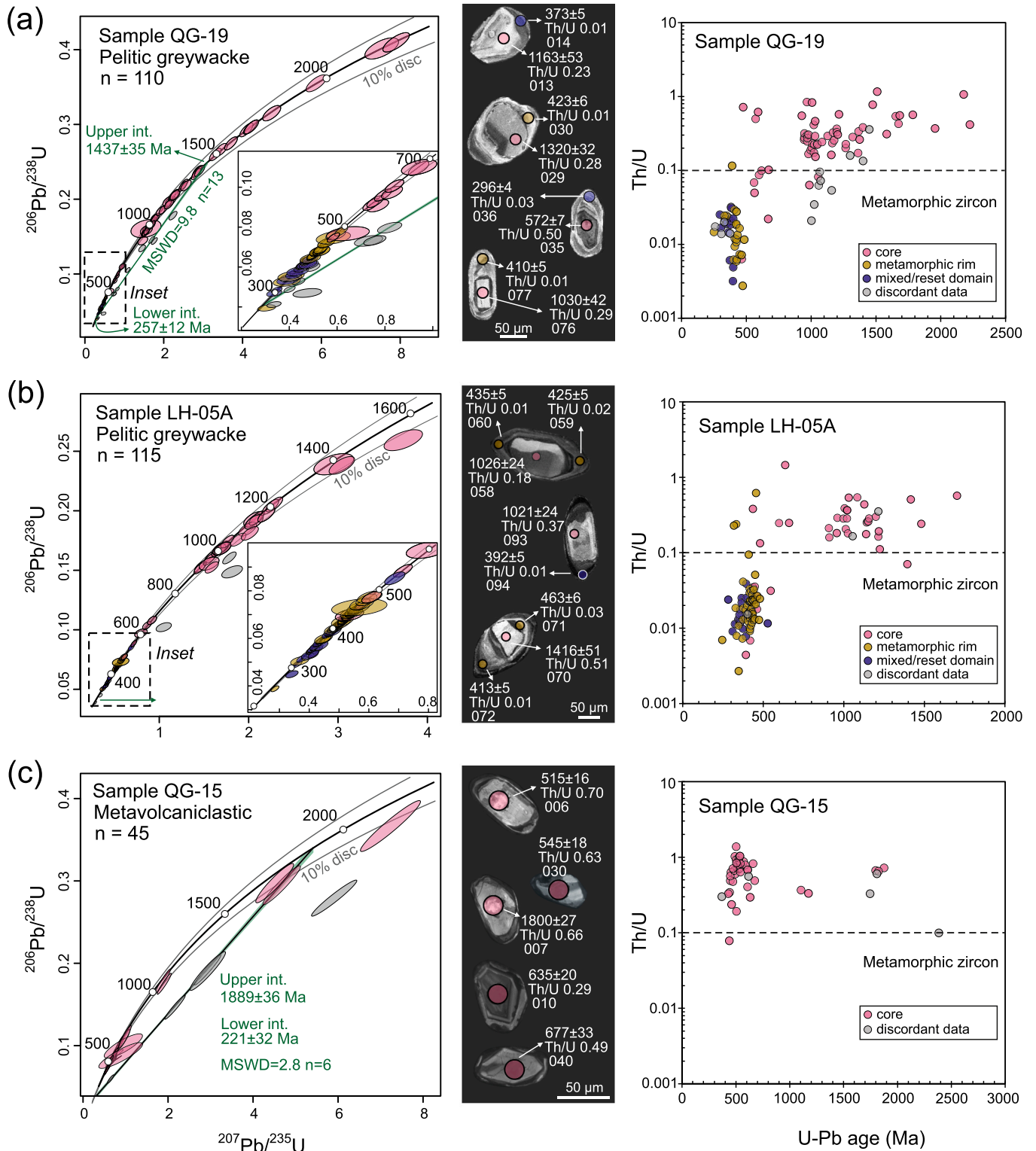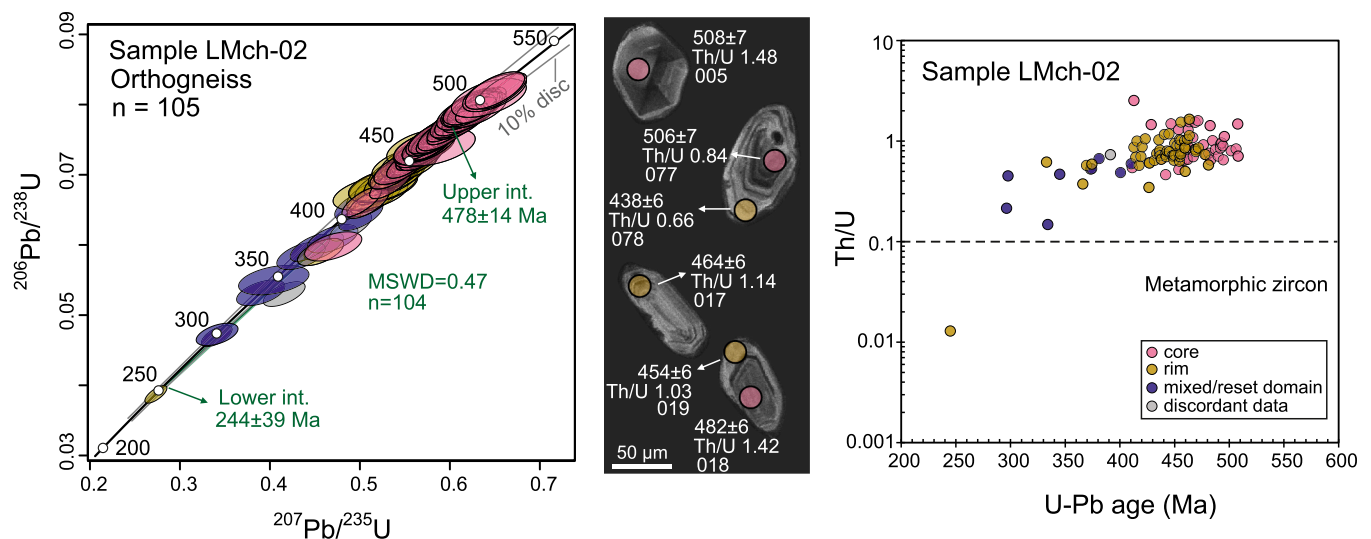
Fig. 4. Wetherill Concordia plots, representative CL images, and Th/U as a function of age plots for measured zircon grains in pelitic-psammitic gneiss samples (a) PET-01, (b) QLl-04, and (c) LMch-01. Circles in CL images indicate the location of laser spots along with U—Pb individual age (±2σ), Th/U ratio, and spot number. Grey ellipses are measurements that exceed the 10% discordance curves. MSWD = Mean Square of the Weighted Deviates for the isochron fit (Vermeesch, 2018 and references therein).

0.7 and 0.5 Ga (36%), 1.3 and 0.9 Ga (31%), and >1.5 Ga (18%) (Fig. 7j). Unfiltered data yield up to 26% of U—Pb ages younger that ca. 500 Ma. Permo–Triassic (260–250 Ma) and Ordovician–Silurian (470–450) U—Pb ages in metamorphic rims and recrystallized domains of zircons from paragneiss are quite similar to crystallization and

metamorphic ages measured in zircons from orthogneisses from the Iglesias Complex (Fig. 7k; van der Lelij et al., 2016, Tazzo-Rangel et al., 2019). U—Pb ages of inherited zircons from orthogneisses are similar to some age modes in KDE diagrams of paragneiss samples.

Fig. 5. Wetherill Concordia plots, representative CL images, and Th/U as a function of age plots for measured zircon grains in pelitic-psammitic gneiss samples (a) QG-19 and (b) LH-05A, and volcaniclastic gneiss sample (c) QG-15. Legend as in Fig. 4.

5.1.1. *Maximum depositional ages (MDAs)*

Several strategies are employed to estimate MDAs of sedimentary rocks using detrital U—Pb ages of zircon. Here we report commonly recommended and probably more successful methods for determining MDAs (see Coutts et al., 2019 and references therein): (1) the youngest graphical peak or mode (YPP) (Dickinson and Gehrels, 2009), (2) the

weighted average of the youngest grain cluster at 2σ (YGC2σ) (Dickinson and Gehrels, 2009) of three or more dates, and (3) the τ ages of Barbeau et al. (2009). The latter calculate the weighted average of all dates whose central values fall between the probability minima surrounding the youngest graphical peak or mode. All ages were calculated using U—Pb dates less than 10% discordant. Detrital grains with similar

Fig. 6. Wetherill Concordia plot, representative CL images, and Th/U as a function of age plot for measured zircon grains in hornblende-orthogneiss of sample LMch-02. Legend as in Fig. 4.

Th/U ratios were selected when defining clusters in the YGC2σ method to independently corroborate that such a detrital zircon population possibly represents a single zircon forming event or source (Spencer et al., 2016).

In the case of the Iglesias Complex, we calculated MDAs for samples with most analyses performed in detrital cores (>70%). Therefore, we excluded samples LH-05A and STPD-56 from calculations. Specific details of the selected single detrital grains for MDA calculations are indicated in the Supplementary Table 1. The pelitic-psammitic paragneiss yielded YPP ages of approximately 533–530 Ma, whereas YGC2σ and τ ages range from 537 ± 7 Ma to 518 ± 8 Ma, as shown in Table 2. An exception is the sample QG-19, yielding MDAs around 580–570 Ma. The hornblende-biotite volcaniclastic paragneiss QG-15 have similar ages, within analytical uncertainty: YPP of ca. 525 Ma, YGC2σ of 507 ± 37 Ma, and τ age of 527 ± 30 Ma.

5.2. Whole-rock geochemistry

Major and trace element compositions of the rock samples analyzed in this work are listed in Table 3. For comparison, geochemical data of metasedimentary rocks from related peri-Gondwanan blocks (the Santander Massif in Colombia and the Maya Block and the Acatlán Complex in south Mexico; Fig. 1a) is plotted with our results from the Mérida Andes. Major elements were recalculated on an anhydrous basis before using them in various indexes and graphics.

Pelitic-psammtic protoliths have variable SiO_2 contents, between 59.5 and 80.0 wt%, and are considered non-calcareous because CaO is less than 4 wt% (Herron, 1988). According to mineralogical and chemical maturity, the SiO_2/Al_2O_3 and K_2O/Na_2O ratios typically indicate different types of sandstones: quartz-arenite sandstones have higher SiO_2/Al_2O_3 than alumina-rich intermediate sandstones, whereas K_2O/Na_2O distinguishes between greywackes and arkoses (e. g., Herron, 1988; Wimmenauer, 1984). Thus, the sedimentary protoliths of the Iglesias Complex are probably between pelite and pelitic-greywacke, with only one sample classified as quartz-rich greywacke (Fig. 8a).

During the weathering, transport, and mixture of different clastic sediments, the content of insoluble elements such as Al, Ti, and Zr may vary, but their relative proportions are usually transferred from the source to the sediments with no modifications (Garcia et al., 1994). In the triangular plot of Al_2O_3-Ti-Zr (Fig. 8b), the metapelitic-metapsammitic rocks of the Iglesias Complex form a linear array between shale and sandstone compositions, with the latter more Zr-rich

due to the zircon concentration in quartzose rocks (Garcia et al., 1994).

The diagram in Fig. 8c depicts intermediate chemical maturity and semi-arid paleoclimate conditions during deposition, expressed as a function of percent of SiO_2 and total percent of Al_2O_3, K_2O, and Na_2O (Suttner and Dutta, 1986). The mineralogy and geochemistry of meta-sediments may reflect the composition of weathering profiles in the source rocks instead of the source itself (e.g., Nesbitt and Young, 1984). The Chemical Index of Alteration (CIA; Nesbitt and Young, 1984) is used to estimate the weathering intensity of the source rocks. The pelitic-psammitic compositions of the Iglesias Complex yield CIA values ranging from 52 to 75, following a weak to moderate weathering trend from granodioritic source rocks (Fig. 8d). The volcanic-volcaniclastic protoliths have an andesitic weathering trend and lower CIA values between 45 and 55, suggesting incorporation of detritus from relatively fresh igneous sources. All samples form a roughly linear array between plagioclase and illite compositions in the A-CN-K triangular plot in Fig. 8d, which may indicate that the relative abundances of Al, Ca, Na, and K are mostly influenced by moderate weathering intensity of plagioclase in the source rocks (e.g., Nesbitt and Young, 1984).

Some compatible and incompatible trace element ratios such as La/Th, La/Sc y Th/Co usually discriminate provenances of sedimentary rocks (e.g., Cullers, 2002; Floyd and Leveridge, 1987; McLennan et al., 1993). Pelitic-psammitic protoliths have Th/Sc above 0.8, which is typical of continental crust sources. In contrast, most volcanic and volcaniclastic protolith samples yield Th/Sc < 0.8, suggesting mantle-derived rocks in the source area. All the diagrams in Fig. 9 are consistent with felsic-intermediate sources and sediment recycling for siliclastic detritus and a mafic trend for volcanic-volcaniclastic protoliths.

Normalized to Post-Archean Australian Shale (PAAS), most of the trace element compositions in pelitic-psammitic protoliths are variable, but still comparable to the average of the upper continental crust (UCC), ranging approximately from 0.5 to 1.5 PAAS (Fig. 10a). Large ion lithophile elements (LILE) like Sr, Ba, and U, display both positive and negative anomalies which can be attributed to variable remobilization during high-grade metamorphism. Positive and negative anomalies in high field strength elements (HFSE) such as Zr and Hf are related to greywacke (Zr-rich) and pelitic compositions (Zr-poor), respectively. Variable concentrations are also noticeable among the transition elements Sc, V, Cr, Co, and Ni.

Rare earth elements (REE) of metapelitic-metapsammitic rocks normalized to chondrites reflect fractionated sources, compositionally similar to UCC and PAAS, with $(La/Yb)_N$ ranging from 3.6 to 15.8
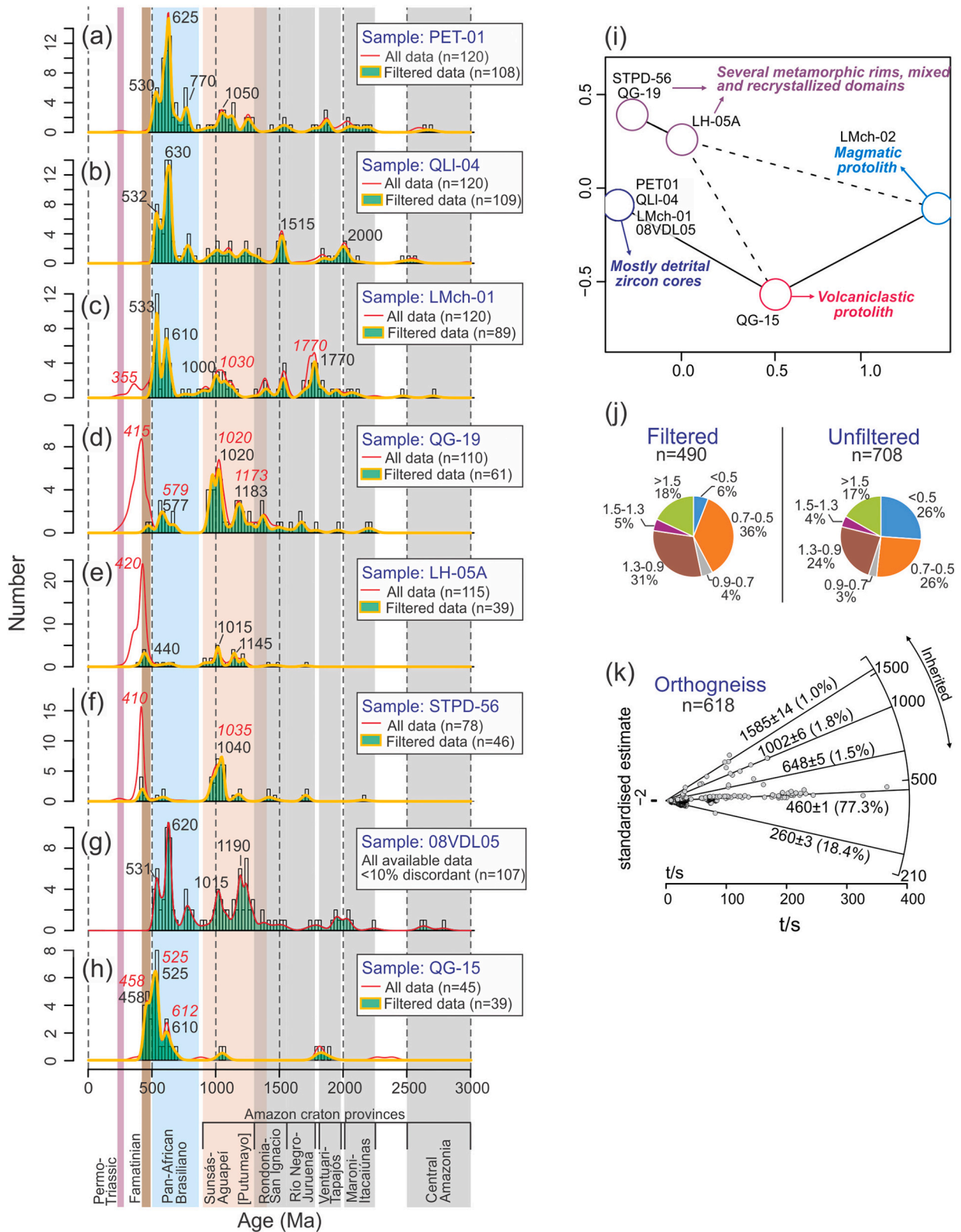
Fig. 7. (a-h) Kernel Density Estimation (KDE) and histogram plots for detrital zircon U—Pb data from the Iglesias Complex, compared to age spectra from potential source regions (references in the text and Fig. 1). Filtered data are analyses >10% discordant and on metamorphic rims and mixed-recrystallized domains. Data in (f) and (g) from Tazzo-Rangel et al. (2019) and van der Lelij et al. (2016), respectively. (i) Multidimensional scaling plot (MDS; Vermeesch, 2013) for filtered detrital zircon U—Pb data. Solid and dashed lines indicate the nearest and second nearest neighbors, respectively. (j) Pie charts of the percentage of detrital zircons in all samples for specific age groups (in Ga), using filtered and unfiltered data. (k) Radial plot (Vermeesch, 2018) for U—Pb ages of zircons in orthogneisses of the Iglesias Complex (data compiled from this study —sample LMch-02—; Tazzo-Rangel et al., 2020, 2019; van der Lelij et al., 2016).

Table 3

Whole-rock geochemistry of metasedimentary rocks and Hbl-orthogneiss of the Iglesias Complex.

Sample	Pelitic-psammitic paragneiss							Volcanic-volcaniclastic paragneiss				Orthogneiss
	LH-01	QLl-04	QMc-01	PET-02	LH-05A	SPTD-56	PET-01	LMX-02	QG-15	MG-11	QP-02	LMch-02
Oxide (wt%)												
SiO_2	67.35	79.07	58.06	67.02	61.88	64.22	56.28	59.77	53.33	56.29	53.37	61.75
Al_2O_3	15.78	9.64	21.03	15.55	15.64	15.53	20.26	15.78	15.53	15.33	16.95	15.69
$Fe_2O_{3(T)}$	6.93	3.49	8.69	6.4	7.03	7.16	10.76	7.91	10.31	8.77	9.65	6.46
MnO	0.166	0.056	0.137	0.094	0.132	0.115	0.30	0.171	0.174	0.157	0.166	0.118
MgO	2.00	1.06	2.68	1.89	3.15	2.96	3.30	3.89	7.42	6.35	6.61	2.69
CaO	1.06	1.03	0.21	1.33	4.04	2.97	0.85	4.51	8.5	7.46	9.08	5.81
Na_2O	2.16	1.9	0.94	2.4	2.58	2.71	1.89	2.16	0.91	1.1	0.85	2.85
K_2O	2.93	1.76	4.78	2.41	2.61	2.68	4.27	1.39	2.05	1.96	1.23	1.86
TiO_2	0.932	0.683	1.034	0.885	0.89	0.955	1.08	1.105	0.823	0.891	0.546	0.669
P_2O_5	0.10	0.14	0.08	0.15	0.22	0.12	0.07	0.19	0.29	0.09	0.08	0.13
LOI	1.19	0.81	2.2	2.27	0.95	1.25	1.31	2.94	0.97	1.56	0.72	1.17
$Total$	100.6	99.63	99.84	100.4	99.11	100.7	100.37	99.83	100.3	99.94	99.26	99.19
Trace element (ppm)												
Sc	16	7	21	16	18	17	24	20	36	31	38	21
Be	2	2	3	2	2	2	-	2	2	5	1	2
V	106	53	139	100	139	127	151	151	260	216	226	136
Cr	480	610	280	290	430	310	282	360	470	460	180	390
Co	17	8	21	16	23	22	25	24	40	35	37	17
Ni	40	20	50	40	50	70	54	50	120	130	20	20
Cu	40	<10	50	60	30	30	20	30	10	<10	<10	10
Zn	90	40	130	80	100	80	133	110	90	90	100	80
Rb	146	66	220	118	108	105	207	63	83	61	62	64
Sr	128	84	65	188	338	255	128	208	230	185	518	288
Y	27.0	30.1	39.5	29.9	25.0	24.0	40.2	24.0	21.1	26.6	13.0	24.0
Zr	180	369	176	285	137	243	180	184	218	74	69	190
Nb	13.9	9.5	18.3	13.8	12.0	12.0	21.2	13.0	9.1	9.2	2.0	8.0
Mo	10	14	4	5	9	5	5	6	4	4	5	9
Cs	6.1	2.3	12.7	1.7	4.3	3.2	7.9	0.8	2.6	2	3.8	1.1
Ba	493	294	758	452	837	615	537	345	580	211	158	757
La	40.8	36.1	53.5	40.7	58.6	34.6	54.9	66.4	22.4	16.3	8.1	30.0
Ce	82.3	76.0	105.0	82.8	118.0	70.4	113.6	131.0	47.8	35.2	18.0	57.9
Pr	9.11	8.34	11.8	9.19	13	8.26	12.95	13.8	5.72	4.17	2.25	6.42
Nd	34.6	31.5	44.4	34.3	48	30.4	50.3	48.1	22	16.4	9.5	25
Sm	6.78	6.45	8.85	6.58	8.80	6.30	9.65	8.30	4.64	3.82	2.30	5.20
Eu	1.38	1.37	1.59	1.49	1.68	1.36	1.67	1.42	1.23	1.24	0.79	1.33
Gd	5.87	5.83	7.48	5.75	6.40	4.90	8.76	5.50	4.26	4.45	2.60	4.70
Tb	0.89	0.92	1.16	0.90	0.90	0.80	1.28	0.70	0.67	0.80	0.40	0.70
Dy	4.96	5.30	6.88	5.28	5.30	4.60	8.13	4.40	3.89	4.97	2.50	4.60
Ho	0.90	1.03	1.34	1.01	1.00	0.90	1.63	0.90	0.76	0.94	0.50	0.90
Er	2.50	2.96	3.95	2.93	2.80	2.90	4.77	2.80	2.09	2.55	1.50	2.50
Tm	0.36	0.43	0.58	0.44	0.41	0.43	0.66	0.41	0.31	0.35	0.22	0.37
Yb	2.43	2.94	3.73	2.97	2.50	2.90	4.63	2.80	2.04	2.02	1.40	2.60
Lu	0.36	0.46	0.57	0.45	0.36	0.45	0.70	0.42	0.30	0.30	0.22	0.39
Hf	4.9	9	4.9	7.5	2.8	6.5	5.5	3.9	6.3	2	1.5	3.8
Ta	1.00	0.91	1.39	0.97	0.90	0.90	1.39	1.00	0.51	0.66	0.30	0.70
Pb	21	21	20	15	14	15	19	17	7	8	8	12
Th	11.8	10.0	16.4	14.6	15.1	9.6	18.4	27.7	6.8	3.9	1.8	8.3
U	2.53	2.87	3.89	2.39	2.10	1.40	3.36	1.90	1.73	1.31	0.60	1.20
Parameters and ratios[a]												
CIA[b]	65	59	75	64	52	55	69	55	45	47	47	48
SiO_2/Al_2O_3	4.27	8.20	2.76	4.31	3.96	4.14	2.78	3.79	3.43	3.67	3.15	3.94
K_2O/Na_2O	1.36	0.93	5.09	1.00	1.01	0.99	2.26	0.64	2.25	1.78	1.45	0.65
Zr/Al_2O_3	11.34	37.83	8.17	17.99	8.60	15.56	8.78	11.30	13.94	4.75	4.01	11.87
$(La/Yb)_N$[c]	11.32	8.28	9.67	9.24	15.80	8.04	8.00	15.99	7.40	5.44	3.90	7.78
$(La/Sm)_N$[c]	3.79	3.52	3.80	3.89	4.19	3.45	3.58	5.03	3.04	2.68	2.22	3.63
$(Gd/Yb)_N$[c]	1.90	1.60	1.60	1.60	2.10	1.40	1.50	1.60	1.70	1.80	1.50	1.50
Eu/Eu*[c]	0.67	0.68	0.6	0.74	0.68	0.75	0.56	0.64	0.85	0.92	0.99	0.82
ΣREE	193.2	179.6	250.8	194.8	267.8	169.2	273.7	287.0	118.1	93.5	50.3	142.6
Th/Sc	0.74	1.43	0.78	0.91	0.84	0.56	0.76	1.39	0.19	0.13	0.05	0.40
La/Th	3.46	3.61	3.26	2.79	3.88	3.60	2.99	2.40	3.30	4.15	4.50	3.61
La/Sc	2.55	5.16	2.55	2.54	3.26	2.04	2.27	3.32	0.62	0.53	0.21	1.43
Th/Co	0.69	1.25	0.78	0.91	0.66	0.44	0.74	1.15	0.17	0.11	0.05	0.49
Zr/Sc	11.25	52.71	8.38	17.81	7.61	14.29	7.43	9.20	6.06	2.39	1.82	9.05

[a] LOI-corrected in oxides.

[b] Chemical index of alteration (Nesbitt and Young, 1984). CIA = $[Al_2O_3/(Al_2O_3 + CaO* + K_2O + Na_2O)] \times 100$. CaO*: CaO corrected for apatite using P_2O_5.

[c] Normalized to chondrites (Boynton, 1984). Eu/Eu* = $Eu_N/(Sm_N*Gd_N)^{1/2}$.
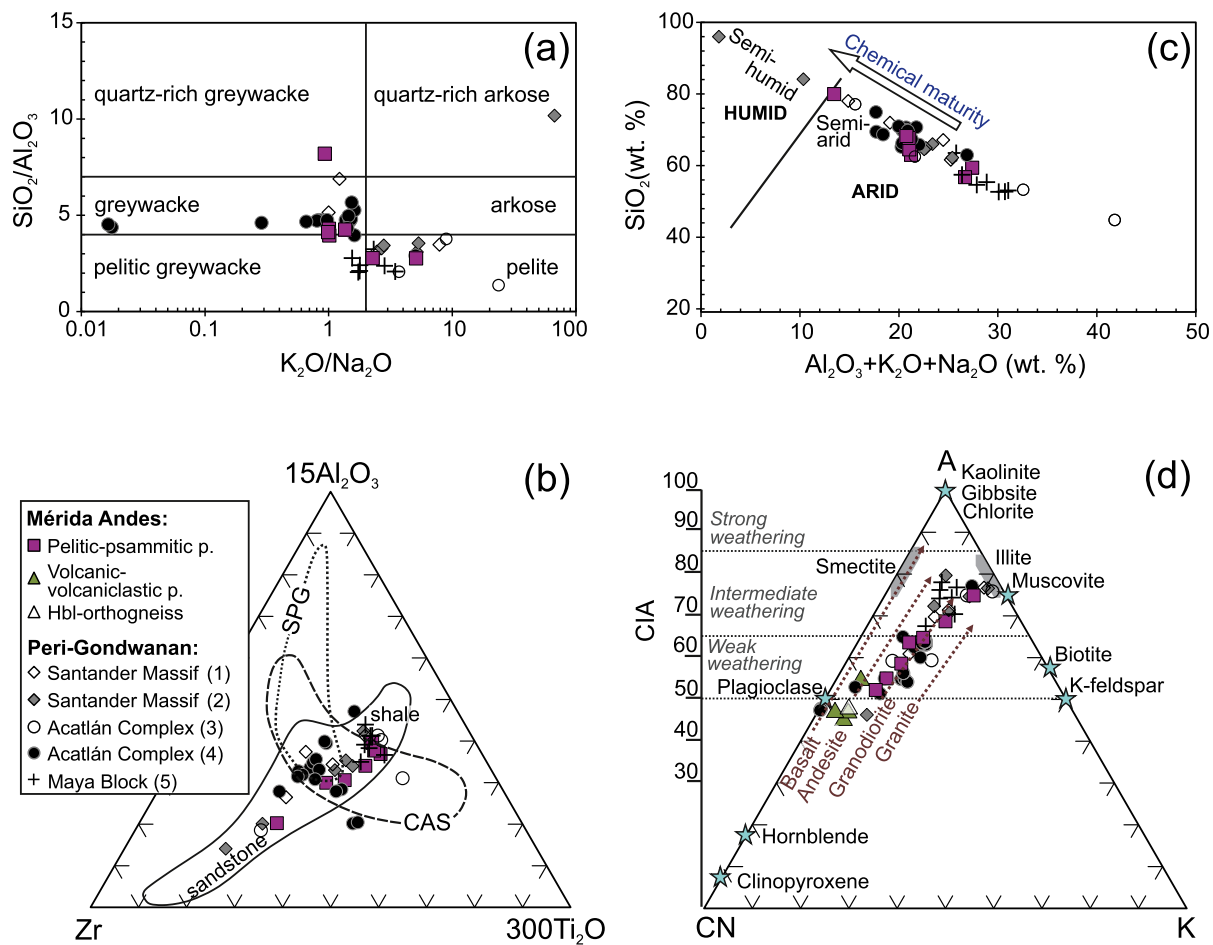
Fig. 8. (a) SiO_2/Al_2O_3 vs. K_2O/Na_2O (Wimmenauer, 1984) and (b) Al_2O_3-Zr-Ti (Garcia et al., 1994) plots for compositional classification of pelitic-psammitic gneisses. CAS: Calc-alkaline suite. SPG: Strongly peraluminous granites. (c) SiO_2 vs. $Al_2O_3 + K_2O + Na_2O$ plot (Suttner and Dutta, 1986) depicting chemical maturity and paleoclimate of the analyzed rocks. (d) A-CN-K plot indicating weathering profiles of sources and the Chemical Index of Alteration (CIA) (Nesbitt and Young, 1984). Geochemical data from Peri-Gondwanan terranes after (1) Mantilla-Figueroa et al., (2016a), (2) García-Ramírez et al. (2019), (3) Dostal and Keppie (2009), (4) Ortega-Obregon et al. (2010), (5) González-Guzmán et al. (2016a).

(Fig. 10b). Relatively flat REE patterns have $(Gd/Yb)_N$ between 1.15 and 2.1. Volcanic and volcaniclastic protoliths show similar fractionation patterns, although less REE-enriched. Variable fractionation of plagioclase during weathering is inferred from Eu/Eu* between 0.60 and 0.99. The trace element composition normalized to the primitive mantle in metasedimentary pelites and psammites is similar to UCC (Fig. 10c), with enrichment in LILEs in comparison with HSFEs. Volcanic-related rocks are relatively less enriched in LILEs and HSFEs compared to siliciclastic protoliths. Chemical classifications based on major oxides and trace elements suggest basaltic to andesitic calk-alkaline compositions for volcanic-volcaniclastic protoliths and hornblende-orthogneiss (Fig. 11).

5.3. Nd—Hf isotope geochemistry

Metasedimentary rocks of the Iglesias Complex have negative εNd_{530Ma} between −12.5 and −3.8 for pelitic-psammitic compositions, whereas volcaniclastic protoliths are more radiogenic with εNd_{530Ma} from −3.6 to −0.7 (Table 4; Fig. 12a-c). All rock samples yielded crustal residence ages ($T_{DM(Nd)}$) spanning from ~1.8 to ~1.3 Ga, except two pelitic-psammitic samples (QMc-01, PET-01) that have $T_{DM(Nd)}$ of ~2.3 Ga (Table 4; Fig. 12a,b). Such rocks are Al-rich muscovite-sillimanite bearing gneisses. $^{147}Sm/^{144}Nd$ values of 0.10–0.13 in siliciclastic protoliths are typical of crustal rocks, although amphibolite-biotite volcaniclastic gneisses vary between 0.10 and 0.14. One para-amphibolite

yielded the less differentiated composition, with $^{147}Sm/^{144}Nd$ of 0.15.

Volcanic and volcaniclastic rocks are less enriched in quartz and plot between average upper crust and arc andesite in the Th/Sc vs εNd_t diagram of Fig. 12c. Highly variable Th/Sc suggest heterogeneous and less differentiated sources (McLennan et al., 1993). In contrast, siliciclastic detritus in pelitic-psammitic protoliths have lower εNd_t (older provenance) and relatively uniform Th/Sc of approximately 0.8, similar to the upper crust (Rudnick and Gao, 2013; Taylor and McLennan, 1985).

εHf_t values are comparable to εNd_t but volcanic-volcaniclastic gneisses yielded more radiogenic compositions with εHf_{530Ma} up to +3.4 (Table 4; Fig. 12d). Accordingly, $T_{DM(Hf)}$ ranges from ~2.0 to ~1.5 Ga in pelitic-psammitic protoliths, and from ~1.5 to ~1.2 Ga in volcaniclastic protoliths. The $^{176}Lu/^{177}Hf$ is quite variable, yielding values of 0.008–0.011 in more siliceous paragneisses, typical of felsic provenance, and 0.017–0.018 in garnet-bearing or sillimanite-muscovite-bearing rocks. Volcanic and volcaniclastic protoliths also have variable $^{176}Lu/^{177}Hf$: 0.007–0.011 in samples with more felsic components, and 0.017–0.022 in intermediate to mafic compositions (Table 4).

In the εNd_t vs. εHf_t diagram of Fig. 12e, most samples plot close to the terrestrial array of marine sediments, which includes terrigenous and volcaniclastic turbidites, as well as some pelagic clays (e.g., Vervoort et al., 2011). The Nd—Hf isotopic composition of most samples from the Iglesias Complex are explained by a mixture between approximately 25–55% average MORB basalt and 45–75% of average UCC, where volcanic and volcaniclastic protoliths incorporated more juvenile or
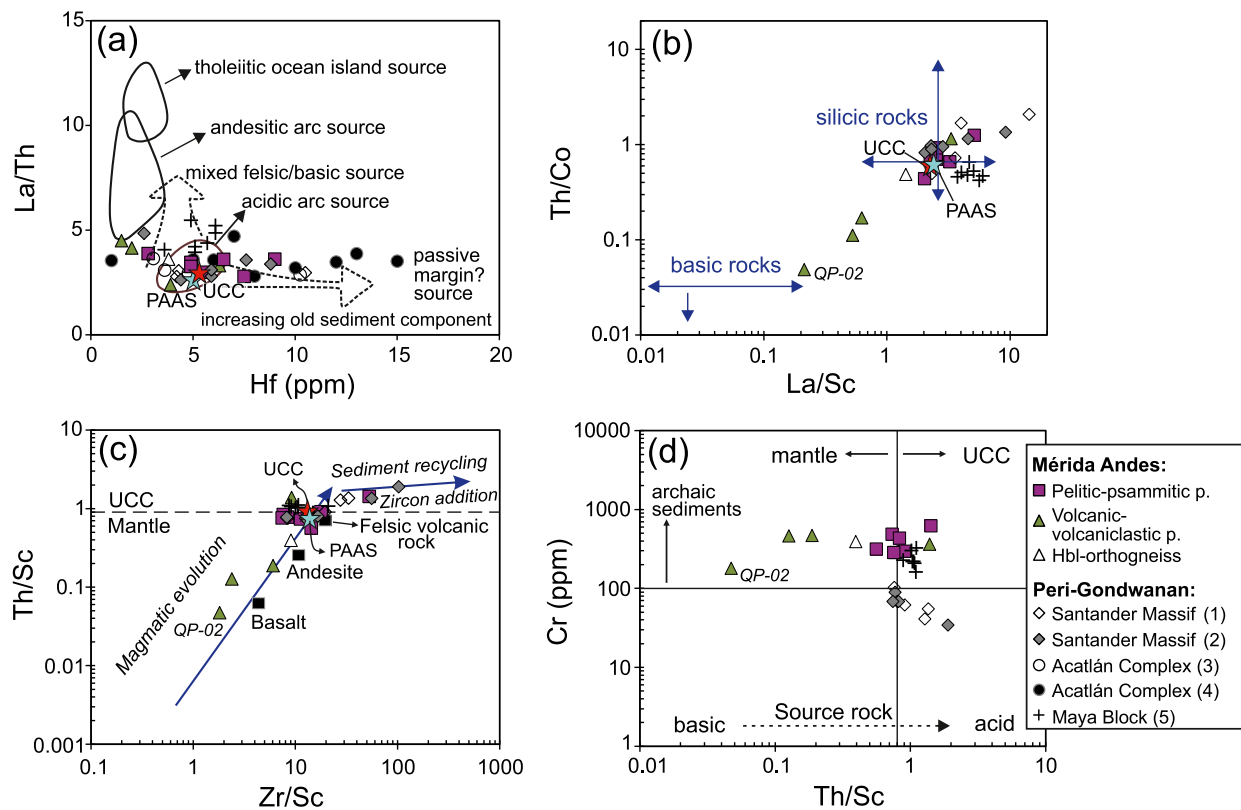
Fig. 9. Source composition of pelitic-psammitic and volcanic-volcaniclastic protoliths of the Iglesias Complex, based on incompatible and compatible trace element ratios plots: (a) La/Th vs. Hf (Floyd and Leveridge, 1987), (b) Th/Co vs. La/Sc (Cullers, 2002), (c) Th/Sc vs. Zr/Sc (McLennan et al., 1993), and (d) Cr vs. Th/Sc after Jenchen (2018) and classifications of McLennan et al. (1993). Hornblende orthogneiss of sample LMch-02 is also shown. Geochemical data from Peri-Gondwanan terranes as in Fig. 8. Compositions of the Upper Continental Crust (UCC) and the Post-Archean Australian Shale (PAAS) reservoirs are from Rudnick and Gao (2013) and Taylor and McLennan (1985), respectively.

mantle-derived material (Fig. 12e). However, the samples QMc-01 and PET-02 deviate from both the terrestrial array and the MORB-UCC hypothetical mixing curve, reflecting different fractionation trends for Sm—Nd and Lu—Hf during sedimentary processes in deep seawater, and therefore, different isotopic signature in the sedimentary rocks (e.g., Chen et al., 2013; Vervoort et al., 2011). Decoupling of the Lu—Hf from the Sm—Nd system resulting in higher radiogenic ^{176}Hf relative to the corresponding ^{143}Nd on the terrestrial trend are a consequence of HREE enrichment in clays (e.g., Nebel et al., 2011; Vervoort et al., 2011).

In a mixture between the most radiogenic amphibolite (QP-02) as an endmember of basaltic-andesitic magmatism (εHf$_{(530\ Ma)}$ = +1.7 and εNd$_{(530Ma)}$ = −0.9), and the less radiogenic pelitic-greywacke gneiss (PET-02) as an endmember of recycled crustal components (εHf$_{(530\ Ma)}$ = −12.1 and εNd$_{(530Ma)}$ = −12.0), most samples plot close to the hypothetical mixing curve (Fig. 12e), suggesting that clastic detritus in paragneisses probably incorporated more than 75% of intermediate-mafic sources, with exception of two samples that are highly recycled.

Deviations of εHf$_t$ and εNd$_t$ from the terrestrial array is quantified as ΔHf$_t$ = εHf$_t$ − [1.55εNd$_t$ + 1.21] (Vervoort et al., 2011). Pelitic and psammitic protoliths yield variable ΔHf$_t$, between +2.9 to +11.9, whereas volcanic-volcaniclastic protoliths have lower and less variable values of ΔHf$_t$, from +1.8 to +5.5. The zircon effect is another approach used to identify volcaniclastic and terrigenous trends, given that variable proportions of this mineral in the sediments influence the Nd—Hf isotopic correlation (e.g., Carpentier et al., 2009; Vervoort et al., 2011). Sediments with excess zircon have Zr/Al$_2$O$_3$ higher than UCC or arcs, but also negative ΔHf$_t$. Sediments lacking in zircon have lower Zr/Al$_2$O$_3$ and positive ΔHf$_t$. All samples analyzed from the Iglesias Complex display positive ΔHf$_t$ values as well as chemical signatures of mixed immature arc terranes and continental provenance in Fig. 12f. Two

volcanic-volcaniclastic paragneisses have the lowest Zr/Al$_2$O$_3$, plotting near the arc rocks composition.

6. Discussion

6.1. Sedimentary sources and timing of deposition

Detrital fractions in the analyzed samples show major age modes in the spectra at ca. 1050–1000 Ma, 630–610 Ma, and 530 Ma, and minor modes at ca. 2000 Ma, 1800 Ma, and 1500 Ma (Fig. 7). Major age modes are consistent with sources from the Putumayo-Oaxaquia basement (e. g., Ibañez-Mejia, 2020; Ortega-Gutiérrez et al., 2018), the Sunsás-Aguapeí orogen (e.g., Teixeira et al., 2010 and references therein) and the Brasiliano-Pan-African belts (Fig. 1 and Fig. 14b).

Brasiliano-Pan-African zircons are probably sourced in granitoids from the Brazilian Araguaia belt (650–500 Ma; e.g., Alves et al., 2019), Gurupi belt (550–500 Ma; e.g., Klein et al., 2020; Palheta et al., 2009), Borborema province (630–540 Ma; e.g., Oliveira et al., 2015), Brasília belt (670–620 Ma, e.g., Pimentel, 2016 and references therein), and the West Africa Hoggar and Dahomey belts (630–580 Ma; e.g., Schmitt et al., 2018 and references therein), all formed during collisional and post-collisional stages of the amalgamation of the Gondwana supercontinent (Fig. 14b; see revision by Schmitt et al., 2018).

A significant detrital population indicates provenances from the Río Negro-Juruena (1890–1600 Ma) and the Rondonia-San Ignacio (1590–1300 Ma) provinces of the Amazon craton. Minor detrital constituents are probably sourced from the Ventuari–Tapajós and Maroni–Itacaiúnas provinces (2260–1800 Ma), whereas only six zircon cores yielded concordant U—Pb ages >2.6 Ga, from the Central Amazonia region (e.g., Cordani and Teixeira, 2007). Equivalent units of ca.
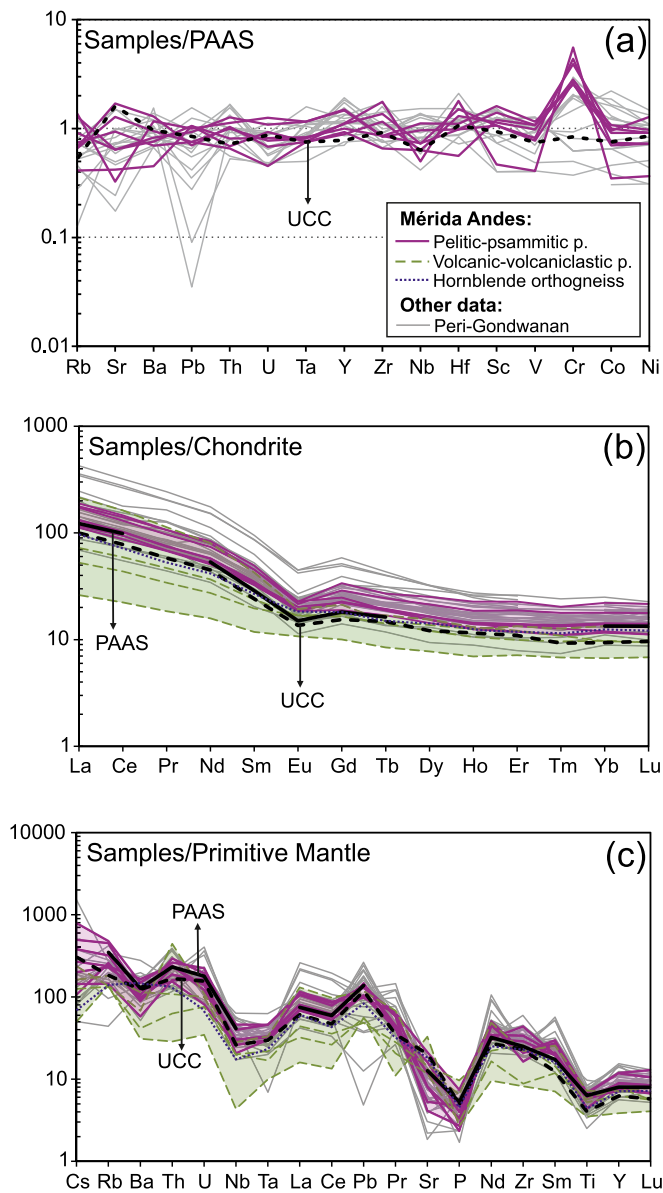
Fig. 10. (a) Trace elements normalized to PAAS (Taylor and McLennan, 1985), (b) Rare Earth Elements (REE) normalized to chondrites (Boynton, 1984), and (c) trace elements normalized to the primitive mantle (Lyubetskaya and Korenaga, 2007) for analyzed rocks of the Iglesias Complex and similar rocks in peri-Gondwanan terranes (references in Fig. 8). UCC and PAAS after Rudnick and Gao (2013) and Taylor and McLennan (1985), respectively.

2.1–1.2 Ga in the Guiana Shield (Kroonenberg, 2019) are also probable sources of Proterozoic zircons.

The smaller number of zircon cores analyzed in samples QG-19, LH-05A, STPD-56, and QG-15 hampers the use of statistical methods for direct population comparison and calculations of MDAs. However, visual inspection of the spectra for each of these samples (Fig. 7) shows some similarities in age ranges, indicating equivalent sources involved in the derivation of the sedimentary precursors.

The constraint on the maximum age of deposition of the Iglesias Complex metasedimentary rocks is ca. 540–530 Ma (Table 2). Such an early Cambrian age is relatively contemporaneous with the 518.7 ± 2.5 Ma age (youngest cluster of five statistically equivalent analyses) obtained from a paragneiss sample collected 37 km southwest of our study area (Fig. 1b) by van der Lelij et al. (2016). Only one sample, QG-19, lacks of early Cambrian detrital zircon grains, suggesting a possible

late Neoproterozoic maximum depositional age at ca. 580 Ma but this age can be biased by an insufficient number of analyzed detrital zircon cores, or simply by the absence of early Cambrian igneous rocks in the catchment zone during time of deposition.

Late Neoproterozoic to Cambrian ages obtained from zircon cores of the paragneisses from the Iglesias Complex are within the 10% range of discordance considered in this study (Fig. 4-6). However, there are concerns about whether these ages represent (1) crystallization ages of 630–530 Ma source rocks or (2) mixed ages due to variable degrees of Pb-loss in older zircons during post-depositional early Paleozoic and Permo–Triassic high-grade metamorphism (Tazzo-Rangel et al., 2020, 2019). Nevertheless, the oldest crystallization age of orthogneiss units intruding metasedimentary gneisses in the Central Mérida Andes yielded a late Cambrian age of 487 ± 7 Ma (Tazzo-Rangel et al., 2019; van der Lelij et al., 2016). Additionally, the hornblende-orthogneiss sample LMch-02, yielding an upper intercept age of 478 ± 14 Ma (Fig. 6), probably represents former tonalitic dykes or sills that intruded the sedimentary sequence, and were later deformed during the Ordovician–Silurian or Permo–Triassic metamorphic events. Therefore, late Cambrian magmatism constrains the minimum depositional age of these paragneisses. Likewise, sample LMch-02 displays geochronological, chemical, and isotopic similarities to other volcanic-volcaniclastic rocks analyzed in this study (Fig. 7i; Fig. 8-12), suggesting comparable magmatic sources.

The climax of the early Paleozoic Famatinian Orogeny is relatively well established in western South America, from Argentina to Venezuela, at ca. 480–470 Ma (e.g., Ramos, 2018 and references therein). Since the Iglesias Complex was metamorphosed during the Famatinian orogeny, the sedimentation of paragneiss protoliths is constrained from ca. 530 Ma to ca. 500 Ma. If such early Cambrian U—Pb ages are indeed a consequence of Pb-loss, then time of deposition might be late Ediacaran, around 580–570 Ma.

Paleo- to Mesoproterozoic Sm—Nd and Lu—Hf crustal residence ages (~1.8–1.3 Ga) suggest a mixture of recycled Rodinia-type basement (Putumayo-Oaxaquia), the Amazon craton, and Pan-African-Brasiliano belts crust (Fig. 12a-c). A few older crustal residence ages of ~2.0 Ga in sillimanite-muscovite paragneiss probably reflect Al-rich pelitic protoliths, perhaps sourced in the Eastern Guiana shield (Fig. 12a) and older distant areas in Central Amazonia. On the other hand, whole-rock isotope systematics reveal a clear trend towards an increasing input from depleted sources for gneisses with dominantly volcanic-related protoliths.

Field evidence as well as geochemical and isotopic signatures indicate two types of metasedimentary rocks of the Iglesias Complex: Pelitic-psammitic and volcanic-volcaniclastic protoliths. The chemical composition of pelite-greywacke paragneisses suggests that they incorporated a wide variety of clastic sediments with variable sorting, maturity, and weathering intensity. Siliciclastic sediments were derived from felsic to intermediate sources with granitic to granodioritic compositions (Fig. 8d) in the Amazon craton and Pan-African-Brasiliano belts. Basaltic to andesitic protoliths suggesting either lava flows or subvolcanic sills (Sample QP-02; Fig. 3d), display typical chemical and isotopic arc signatures, whereas volcaniclastic protoliths possibly represent a mixture of eroded mafic-intermediate volcanic detritus and siliciclastic sediments (Fig. 9d, Fig. 11, Fig. 12f). The lack of late Ediacaran–early Cambrian magmatic rocks in northwestern Gondwana may imply that volcanic-volcaniclastic protoliths are sourced from an incipient or immature arc activity, suggesting the initiation of subduction of the Iapetus Ocean beneath northwestern Gondwana after 530 Ma and before 500 Ma (Fig. 14b).

6.2. Correlation with other peri-Gondwanan blocks

Several crustal fragments adjacent to northwestern Gondwana during the Paleozoic host an Ediacaran-Cambrian basement, mostly composed of metasedimentary sequences and amphibolite, intruded by
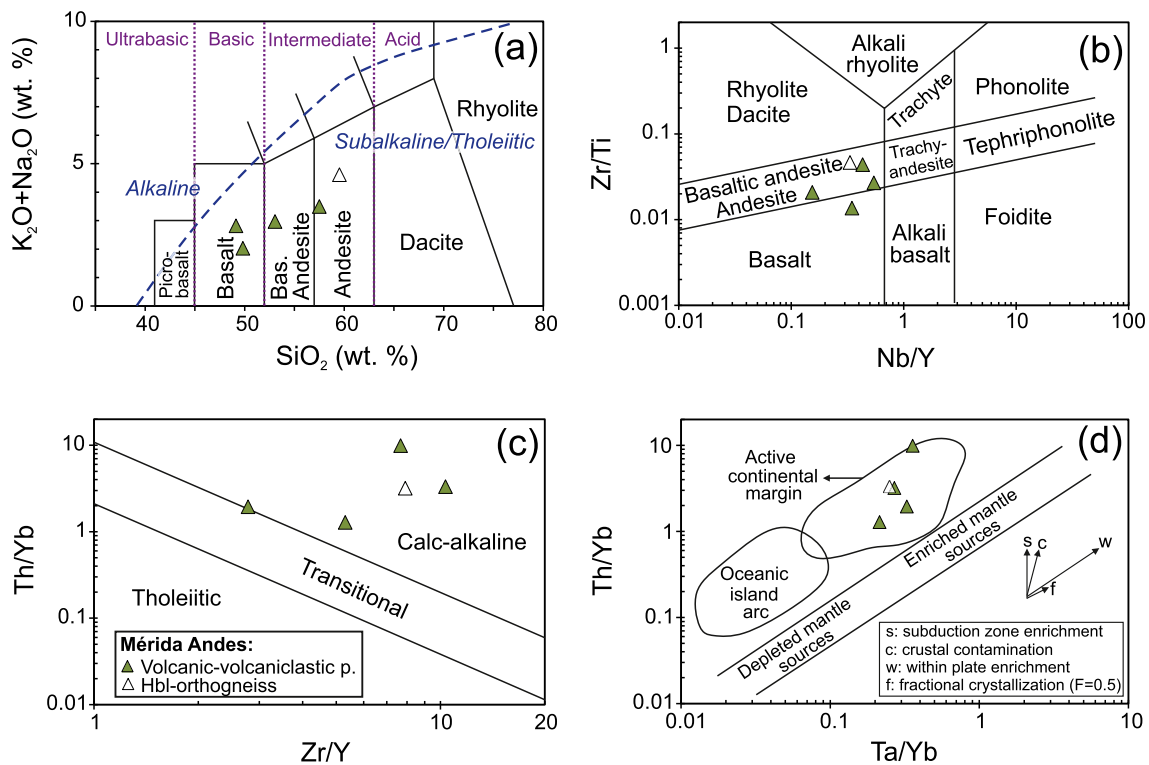
Fig. 11. Geochemistry of volcanic-volcaniclastic paragneisses and hornblende-orthogneiss of the Iglesias Complex. (a) TAS classification diagram (Le Bas et al., 1986). (b) Zr/Ti vs. Nb/Y classification plot (Pearce, 1996 and references therein). (c) Th/Yb vs. Zr/Y plot for discrimination of magmatic series (Ross and Bédard, 2009). (d) Th/Yb vs. Ta/Yb plot as a proxy for crustal contamination in volcanic arc basalts (Pearce, 1983).

Ordovician–Silurian and Permo–Triassic felsic and mafic plutons (see revision by Tazzo-Rangel et al., 2019 and references therein). Fig. 13 depicts KDE plots for detrital zircon U–Pb data from gneissic-schistose rocks of the Mérida Andes in Venezuela, the Santander Massif and the Anacona Terrane in Colombia, the El Oro Complex in Ecuador, the Maya Block in southern Mexico, Guatemala, and Belize, the Chortís Block and the Chuacús Complex in Guatemala, and the Acatlán Complex in southern Mexico (references in caption of Fig. 13). In addition, the unmetamorphosed Cambrian–Ordovician sandstones of the Tiñu Formation in Oaxaquia are included (Gillis et al., 2005).

Visual inspection of the age spectra, CAD curves and clustering in MDS plots suggests broadly similar U—Pb age distributions of detrital zircons in metasedimentary rocks from the Mérida Andes, the Santander Massif and the Las Minas, Otate, Mal Paso, and Amate units of the Acatlán Complex (Fig. 13a,b,i,k,l). The youngest detrital populations in these units yield ages between ca. 560 and ca. 480 Ma, suggesting a late Ediacaran–early Ordovician depositional age for the sedimentary protoliths. Probable equivalent rock units outcrop in the Quetame Massif in the Eastern Cordillera of Colombia (Fig. 14a), where Early Ordovician granitic rocks intruded Cambrian quartzites and phyllites at 483 ± 10 Ma (Horton et al., 2010).

On the other hand, similar detrital distribution is also inferred for the Maya Block and the Tiñu Formation in Oaxaquia (Fig. 13e,j,k,l), suggesting equivalent sources in the Oaxacan Complex (e.g., Gillis et al., 2005; González-Guzmán et al., 2016a; Solari et al., 2009). Sedimentary protoliths of the Maya Block sequence were deposited during the Ediacaran opening of the Iapetus Ocean, after Rodinia break-up, probably starting at ca. 600–580 Ma (González-Guzmán et al., 2016a). Sedimentation may have continued until the early Cambrian, given that the Baldy unit in Belize hosts a few Pan-African-Brasiliano zircons of 613–517 Ma (Martens et al., 2010).

Although the post-Ordovician geologic history of the Maya Block and the Mérida Andes is very similar (e.g., Tazzo-Rangel et al., 2019; van der

Lelij et al., 2016; Weber et al., 2018), significant differences are noticeable before ~500 Ma: (1) the Ediacaran metasedimentary rocks of the Jocote unit within the El Triunfo Complex in the Maya Block overlie Stenian-Tonian basement, which is not clearly exposed in the Mérida Andes, (2) detrital zircon distribution displays restricted probability age modes at ca. 1.5, 1.2 and 1.0 Ga (Fig. 13e), and (3) chemostratigrapic data suggest a sedimentation age of 600–580 Ma (González-Guzmán et al., 2016a). The latter may imply that sedimentation of the Jocote unit predates the Iglesias Complex by at least 40 Ma.

Another probable equivalent group in the MDS plot is formed by metasedimentary rocks from the Chortís Block, Neoproterozoic–Ordovician units of the Acatlán Complex, and the Anacona Terrane (Fig. 13c,g,h,l), which are unrelated to detrital zircons from the Mérida Andes. Instead, zircon detrital U–Pb data of the Chuacús Complex and the El Oro Complex may be related to the Mérida Andes as nearest neighbors (Fig. 13l). Metasedimentary rocks of the El Oro Complex hosts Brasiliano zircons of ca. 550–510 Ma, suggesting an early Cambrian MDA. Alternatively, this zircon population is possibly related to igneous sources in the Pampean orogeny of Argentina (Casquet et al., 2018; Suhr et al., 2019).

Geochemical data from the Ediacaran–Cambrian Zacango, Huerta, and Las Minas units of the Acatlán Complex (Dostal and Keppie, 2009; Ortega-Obregon et al., 2010) as well as the Silgará Formation in the Santander Massif (García-Ramírez et al., 2019; Mantilla-Figueroa et al., 2016a) is comparable to the Mérida Andes (Fig. 8-10). Nd isotope evolution lines of the Zacango metasedimentary rocks are remarkably similar to the Iglesias Complex (Fig. 12b). On the contrary, the Baldy and Jocote units from the Maya block have slightly different Nd systematics and dissimilar Hf isotope evolution lines compared to the Mérida Andes (Fig. 12b,d).

Table 4
Sm—Nd and Lu—Hf isotope data for metasedimentary rocks and Hbl-orthogneiss of the Iglesias Complex.

Sample	Sm (ppm)	Nd (ppm)	^{143}Nd/^{144}Nd[a]	2σ	^{147}Sm/^{144}Nd	(^{143}Nd/^{144}Nd)$_t$	εNd$_t$[c]	T$_{DM\,(Nd)}$[d] (Ga)	Lu (ppm)	Hf (ppm)	^{176}Hf/^{177}Hf[e]	2σ	^{176}Lu/^{177}Hf	(^{177}Hf/^{176}Hf)$_t$[b]	εHf$_t$[c]	T$_{DM\,(Hf)}$[f] (Ga)
QMc-01	10.2	53.5	0.511740	0.000091	0.1240	0.511309	−12.5	2.3	0.63	4.94	0.282455	0.000020	0.0182	0.282274	−6.3	2.0
PET-02	7.81	46.2	0.511786	0.000033	0.1301	0.511334	−12.0	2.3	0.43	7.63	0.282188	0.000024	0.0080	0.282108	−12.1	1.8
LH-05A	9.09	51.0	0.512109	0.000034	0.1077	0.511735	−4.2	1.4	0.42	3.49	0.282616	0.000026	0.0172	0.282445	−0.2	1.5
SPTD-56	6.28	33.3	0.512070	0.000023	0.1223	0.511645	−5.9	1.7	0.37	4.81	0.282417	0.000026	0.01010	0.282308	−5.1	1.6
PET-01	9.67	50.3	0.511989	0.000046	0.1162	0.511585	−7.1	1.7	–	–	–	–	–	–	–	–
QLl-04	6.82	35.0	0.511972	0.000030	0.1177	0.511585	−7.5	1.8	–	–	–	–	–	–	–	–
LH-01	7.75	41.2	0.511981	0.000057	0.1136	0.511585	−7.1	1.7	–	–	–	–	–	–	–	–
LMx-02	7.44	45.4	0.512110	0.000022	0.0991	0.511766	−3.6	1.3	0.40	5.36	0.28249	0.000024	0.0106	0.282384	−2.4	1.4
QG-15	4.34	20.2	0.512299	0.000023	0.1301	0.511847	−2.0	1.5	0.30	6.30	0.282529	0.000023	0.0069	0.282461	+0.4	1.2
MG-11	3.82	15.5	0.512358	0.000039	0.1488	0.511841	−2.1	1.7	0.30	2.00	0.282762	0.000022	0.0216	0.282547	+3.4	1.5
QP-02	2.39	10.3	0.512425	0.000027	0.1502	0.511904	−0.9	1.6	0.22	1.90	0.282662	0.000024	0.0165	0.282498	+1.7	1.4
LMch-02	5.13	25.2	0.512340	0.000030	0.1228	0.511938	−1.0	1.3	0.47	5.36	0.282643	0.000030	0.0125	0.282526	+2.0	1.2

[a] During the analytical session in the Triton-TIMS, the La Jolla standard yielded a mean weighted ^{143}Nd/^{144}Nd of 0.511847 ± 0.000028 (2σ, n = 2). Measurements in the Nu-TIMS of the JNdi-1 and the La Jolla standards yielded a mean weighted ^{143}Nd/^{144}Nd of 0.512097 ± 0.000009 (2σ, n = 8) and 0.511838 ± 0.000018 (2σ, n = 4), respectively.

[b] For the calculations of age-corrected isotope ratios, the following present-day Chondritic Uniform Reservoir (CHUR) values were used: ^{143}Nd/^{144}Nd = 0.512630, ^{147}Sm/^{144}Nd = 0.1960, ^{176}Hf/^{177}Hf = 0.282785, ^{176}Lu/^{177}Hf = 0.0336 (Bouvier et al., 2008). t = 530 Ma for metasedimentary rocks and t = 500 Ma for hornblende orthogneiss.

[c] Age-corrected epsilon Nd (εNdt) and epsilon Hf (εHft) are the deviation of (^{143}Nd/^{144}Nd)$_t$ and (^{177}Hf/^{176}Hf)$_t$, relative to CHURt times 10⁴.

[d] Sm-Nd crustal residence ages are calculated using present-day ^{143}Nd/^{144}Nd = 0.513151 and ^{147}Sm/^{144}Nd = 0.219 (Liew and Hofmann, 1988) and λ^{147}Sm = 6.54 × 10$^{−12}$ a$^{−1}$ (Lugmair and Marti, 1978).

[e] The JMC-475 Hf standard solution yielded a mean weighted ^{176}Hf/^{177}Hf value of 0.282149 ± 0.000006 (n = 23). All measured values of ^{176}Hf/^{177}Hf were normalized to the well-accepted ^{176}Hf/^{177}Hf of 0.282160 for JMC-475 (Blichert-Toft et al., 1997).

[f] Lu-Hf crustal residence ages are calculated using present-day depleted mantle value of ^{176}Hf/^{177}Hf = 0.283224 (Vervoort et al., 2000) and ^{176}Lu/^{177}Hf = 0.03836, calculated for εHf = 0 at 4500 Ma by using λ^{176}Lu = 1.867 × 10$^{−11}$a$^{−1}$ (Scherer et al., 2001; Söderlund et al., 2004) after Weber et al. (2012, 2018).

6.3. The latest Ediacaran-earliest Cambrian margin of NW Gondwana

The supercontinent Gondwana was diachronically assembled during the Neoproterozoic–late Cambrian, after convergence and amalgamation of several paleocontinents and smaller crustal fragments along mobile belts (e.g., Schmitt et al., 2018 and references therein). According to late Ediacaran–early Cambrian paleogeographic reconstructions of Gondwana, northwestern South America was positioned near the South Pole, around 60°S (Fig. 14b; e.g., Merdith et al., 2021; Torsvik and Cocks, 2016).

Chemical trends in metasedimentary rocks of the Mérida Andes and equivalent units in peri-Gondwanan terranes suggest semiarid paleoclimate sedimentation, consistent with moderate to high paleolatitudes (Fig. 8c). An illite-trend in the weathering profile of source rocks (Fig. 8d) suggests close relation to river sediments and temperate- to cold-climate weathering at higher latitudes (e.g., Thiry, 2000). The constrained sedimentation at 530–500 Ma falls in an interglacial period, after the Gaskiers and Fauquier glaciations at ca. 580–570 Ma (e.g., Young, 2018 and references therein), favoring rock weathering and transport of sediments.

We propose that sedimentary protoliths of high-grade paragneisses and schists in the Mérida Andes and related terranes were deposited on an extensive late Ediacaran–early Cambrian continental shelf of northwestern Gondwana. A paleo-river system may have existed, draining detritus from the topographic highs in the Pan-African-Brasiliano Orogen, through part of the Amazon Craton (Rondonia-San Ignacio, Río Negro-Juruena, Sunsás) and the Putumayo-Oaxaquia basements, towards the Iapetus Ocean (Fig. 14b). Age spectra of detrital zircons favor sources in the Araguaia, Paraguaia, and Brasília belts of the Pan-African-Brasiliano orogens, suggesting southeast drainage of the fluvial system in the reconstruction of Fig. 14b. Zircon U—Pb ages of granitoids in the Araguaia belt are bracketed between 524 ± 6 Ma and 536 ± 6 Ma (Alves et al., 2019), whereas older zircons of ca. 630–620 Ma are perhaps sourced in orthogneisses and granitic batholiths of ca. 645–630 Ma in the Brasília belt (e.g., Pimentel, 2016; Vinagre et al., 2014). Such trajectory of the river system running west of the present-day Central Amazonia may explain the relatively low zircon proportion from sources older than 1.8 Ga. An affluent further west possibly incorporated zircons from the Pampean batholiths (now located in Argentina), dated between 537 ± 4 Ma and 530 ± 4 Ma (Casquet et al., 2018 and references therein) into the main river catchment. In addition, it is also possible that late Neoproterozoic zircons (ca. 660–580 Ma) in the Iglesias Complex shed from Avalonian Neoproterozoic crust (Fig. 14b) (e.g., Pollock et al., 2009).

The direction of drainage and sediment transfer in Fig. 14b was roughly opposite to the transport currently operating from the Andes cordillera by the Pacific Ocean to the distant Pleistocene Amazon fan in the Atlantic Ocean (Mason et al., 2019). At present, sediments are efficiently transferred over 4000 km across the South American continent. The most abundant detrital fractions in the Amazon fan are Phanerozoic zircons <0.5 Ga from the northern and central Andes Cordillera and Precambrian zircons from the Sunsás basement (Mason et al., 2019). Such detrital distribution is remarkably similar to the late Ediacaran–early Cambrian deposits in northwestern Gondwana, i.e., detrital zircon from distal "Brasiliano mountains" sources are relatively abundant, followed by Meso-Neoproterozoic Putumayo-Oaxaquia belts, and Proterozoic sources in the Amazon Craton.

Late Ediacaran–early Cambrian magmatic rocks are absent in northwestern South America, except for one nepheline syenite dated at 577.8 +6.3/−9 Ma by zircon U—Pb geochronology (Mejía-Arango et al., 2012). Arc magmatism in Venezuela is not recorded before 499.4 ± 2.7 Ma in the Mérida Andes (van der Lelij et al., 2016), at 493.8 ± 5.2 Ma in the El Baúl Massif (Viscarret et al., 2009), and at 511.3 ± 1.8 Ma in the Cordillera de la Costa belt (Sisson et al., 2005). Thus, the onset of accretionary tectonics and the subsequent Famatinian volcanic arc initiated not earlier than ca. 510 Ma in Venezuela. However, incipient
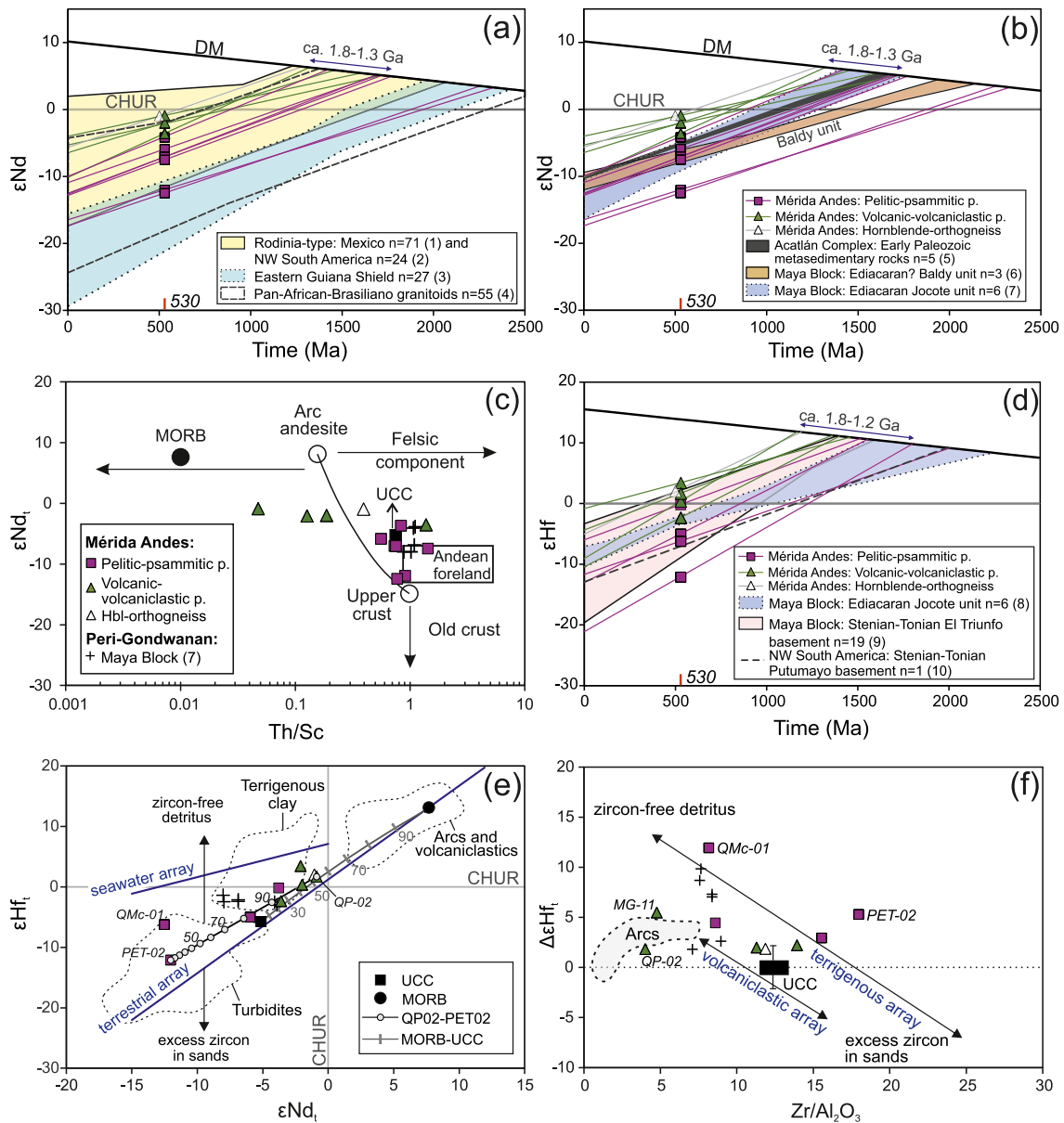
Fig. 12. (a) εNd_t vs. time diagram showing Nd crustal residence ages ($T_{DM(Nd)}$) after Liew and Hofmann (1988) and isotope evolution lines for metasedimentary rocks and orthogneiss from the Iglesias Complex. Composition of potential source regions from (1) Alemán-Gallardo et al. (2019); Patchett and Ruiz (1987); Ruiz et al. (1988); Weber et al. (2018); Weber and Köhler, (1999), (2) Ibañez-Mejia (2020) and references therein; Restrepo-pace et al. (1997), (3) Ibañez-Mejia and Cordani (2020) and references therein, and (4) Alves et al. (2019); Klein et al. (2020); Oliveira et al. (2015); Palheta et al. (2009). (b) As in (a) but compared to peri-Gondwanan Ediacaran-Cambrian metasedimentary rocks: (5) Ortega-Obregon et al. (2010), (6) Weber et al. (2012), (7) González-Guzmán et al. (2016a). (c) εNd_t vs. Th/Sc diagram after McLennan et al. (1993). (d) εHf_t vs. time diagram showing Hf crustal residence ages ($T_{DM(Nd)}$) after Vervoort et al. (2000) (details in footnote of Table 4). Data for comparison: (8) González-Guzmán et al. (2016a), (9) Weber et al. (2018), (10) Ibañez-Mejia and Cordani (2020) and references therein. (e) εNd_t vs. εHf_t diagram. Terrestrial and seawater arrays after Vervoort et al. (2011). Compositions of UCC and MORB in the hypothetical mixing curve are from Chauvel et al. (2014) and Gale et al. (2013), respectively. (f): $\Delta \varepsilon Hf_t$ vs Zr/Al_2O_3 plot from Vervoort et al. (2011). $t = 530$ Ma for metasedimentary rocks and $t = 500$ Ma for hornblende orthogneiss. CHUR model after Bouvier et al. (2008).

subduction of the Iapetus Ocean beneath western Gondwana probably initiated as early as 530 Ma, as suggested by basaltic-andesitic volcanic-volcaniclastic layers intercalated with siliciclastic paragneisses of the Iglesias Complex.

Metasedimentary rocks of the Iglesias Complex are probably correlated to unmetamorphosed Ediacaran–Cambrian fossiliferous sedimentary rocks in the Eastern Venezuela Basin (Hato Viejo and Carrizal formations), the Espino Graben, the El Baúl Massif (Cerrajón and Cañaote formations) (Ostos et al., 2005 and references therein), and in the Arauca Graben in the Colombian foreland basin (e.g., Dueñas-Jiménez and Montalvo-Jónsson, 2020) (Fig. 14a). Fossil content

suggests sedimentation in a shallow marine setting (Dueñas-Jiménez and Montalvo-Jónsson, 2020), probably in a platform environment, as also suggested by Cambrian reconstructions of land and seas in western Gondwana (Torsvik and Cocks, 2016). After trenchward migration and formation of the Famatinian arc during the late Cambrian–Early Ordovician (Oriolo et al., 2021; Ramos, 2018), location of such units far from the subduction trench protected them from deformation and metamorphism (Fig. 14c).
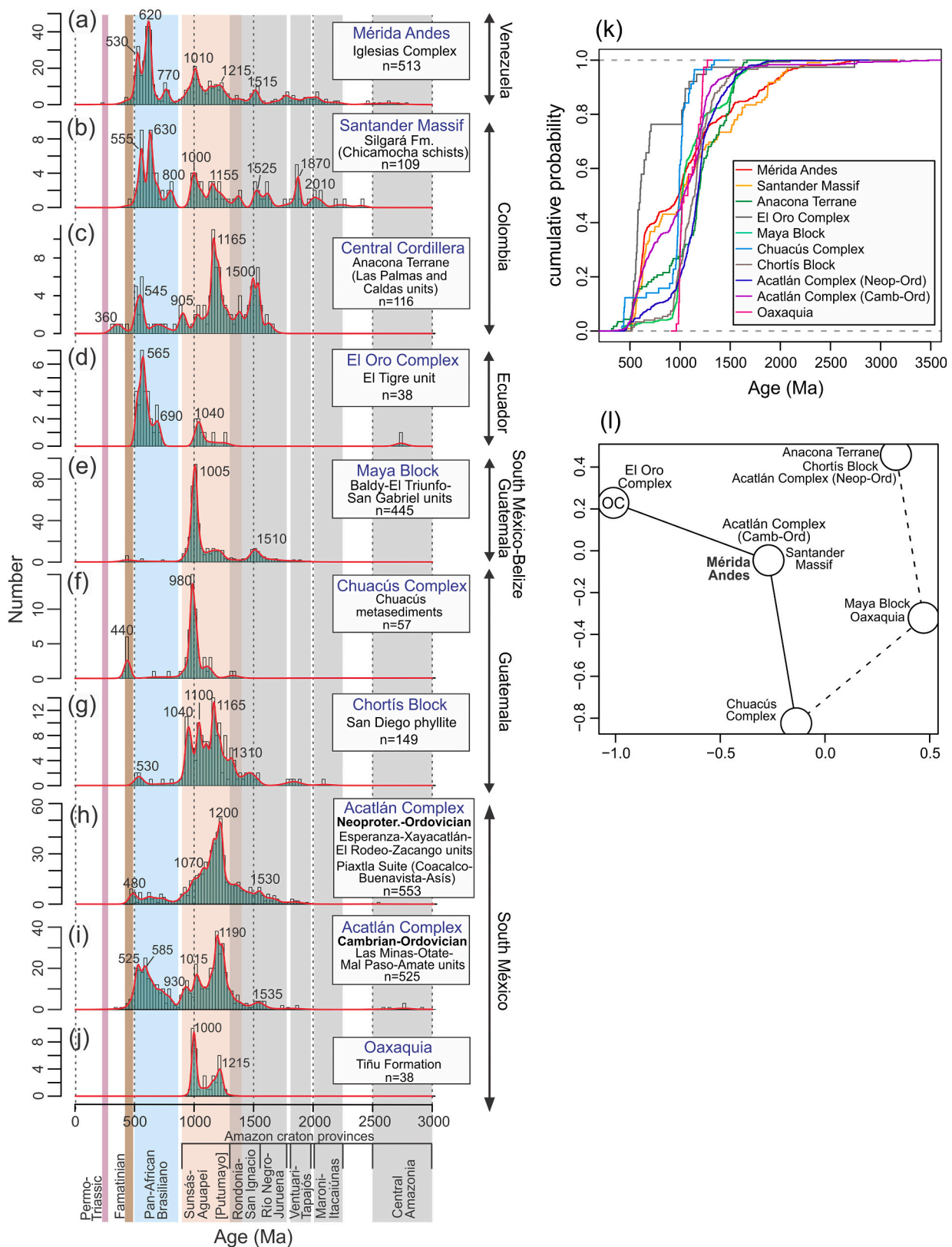
Fig. 13. (a–j) Kernel Density Estimation (KDE) and histogram plots for detrital zircon U—Pb data in peri-Gondwanan Ediacaran-Cambrian metasedimentary units, compared to age spectra from potential source regions (references in the text and Fig. 1). Data compiled from (a) this study; van der Lelij et al. (2016), (b) Mantilla-Figueroa et al., (2016b), (c) Restrepo et al. (2020) and references therein, (d) Suhr et al. (2019), (e) González-Guzmán et al. (2016a); Martens et al. (2010); Solari et al. (2009); Weber et al. (2012), (f-g) Solari et al. (2009); Torres de León et al. (2012), (h) Murphy et al. (2006); Ortega-Obregón et al. (2009); Ramos-Arias and Keppie (2011); Talavera-Mendoza et al. (2005); Vega-Granillo et al. (2007), (i) Galaz et al. (2013); Keppie et al. (2008); Morales-Gámez et al. (2008), (j) Gillis et al. (2005). (k) CAD plot (Vermeesch, 2007) for U—Pb detrital ages in (a-j). (l) MDS plot (Vermeesch, 2013) for detrital zircon U—Pb data in (a-j). Solid and dashed lines indicate the nearest and second nearest neighbors, respectively.
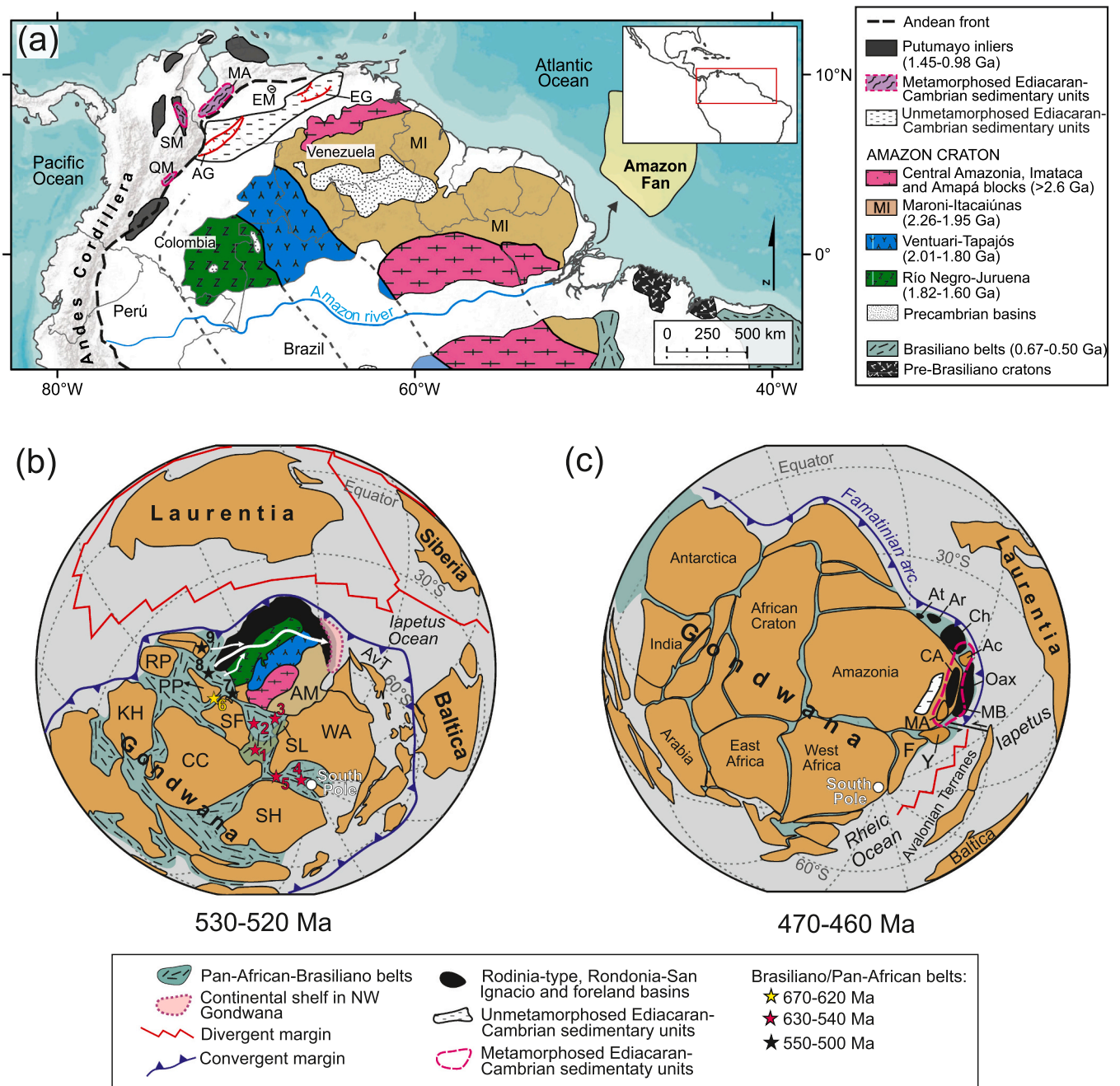
Fig. 14. (a) Location of Ediacaran–Cambrian sedimentary and metasedimentary units in northern South America. Regions of unmetamorphosed units compiled from Dueñas-Jiménez and Montalvo-Jónsson (2020) and Ostos et al. (2005). Amazon fan after Mason et al. (2019). Geochronological provinces of the Amazon craton and Putumayo inliers are also shown (references in Fig. 1). AG: Arauca Graben; EG: Espino Graben; EM: El Baúl Massif, MA: Mérida Andes, QM: Quetame Massif, SM: Santander Massif. (b-c) Simplified paleogeography of the southern hemisphere generated using GPlates 2.2 (https://www.gplates.org/) (Müller et al., 2018). (b) Early Cambrian, using the plate model dataset of Merdith et al. (2021). Arrows indicate the approximate direction of sediment transport. Letters are Gondwanan cratons, whereas stars and numbers indicate Pan-African-Brasiliano mobile belts. AM: Amazonia, CC: Congo, KH: Kalahari, PP: Paranapanema, RP: Río de La Plata, SF: São Francisco, SL: São Luís, SH: Sahara, WA: West Africa. 1: Borborema, 2: Rio Preto; 3: Gurupi, 4: Hoggar, 5: Dahomey, 6: Brasília, 7: Araguaia, 8: Paraguai, 9: Pampean (references in the text). Amazonian provinces as in (a). AvT: Avalonian Terranes. Approximate location of Pan-African-Brasiliano mobile belts after Schmitt et al. (2018). (c) Early Ordovician, according to plate dataset of Scotese (2016). Modifications of peri-Gondwanan terranes and blocks from Weber et al. (2018). Ac: Acatlán; Ar: Arequipa; At: Antofalla, CA: Colombian Andes, Ch: Chortís Block, F: Florida, MA: Mérida Andes, MB: Maya Block, Oax: Oaxaquia, Y: Yucatán.

7. Conclusions

- Metasedimentary gneiss and schist of the Iglesias complex of the Mérida Andes in Venezuela comprise pelitic-psammitic and volcanic-volcaniclastic protoliths. Detrital zircon U—Pb geochronology suggests provenance from Pan-African-Brasiliano belts as well as from sources in the Amazon Craton and the Oaxaquia-Putumayo basement. Reworking of such sources is also reflected in Nd—Hf crustal residence ages of ca. 2.0–1.3 Ga. The time of sedimentation is bracketed between maximum depositional ages at 540–530 Ma and the oldest igneous rocks intruding the paragneiss at ca. 490 Ma.

- Pelitic-greywackic protoliths incorporated clastic sediments derived from felsic to intermediate sources. On the other hand, basaltic to andesitic inputs are probably related to subvolcanic sills or lava

flows, as well as eroded detritus from an incipient arc, suggesting the initiation of subduction of the Iapetus Ocean beneath northwestern Gondwana at ca. 530 Ma. Sedimentary protoliths probably were deposited during the latest Ediacaran–earliest Cambrian on an extensive continental shelf, fed by detritus draining from the topographic highs in the Pan-African-Brasiliano belts, across the Amazon craton, and into the Iapetus Ocean.

- High-grade metasedimentary rocks from the Mérida Andes show similarities with equivalent units in Peri-Gondwanan crustal fragments in the Acatlán Complex and the Santander Massif but no correlation with Ediacaran metasedimentary units in the Maya Block. Correlations are also possible with Ediacaran–Cambrian fossiliferous sedimentary rocks in the Eastern Venezuela Basin and in the Colombian foreland basin. Such units remained unmetamorphosed as their location was far from the subduction trench during the Early Ordovician climax of the Famatinian orogeny.

Supplementary data to this article can be found online at https://doi.org/10.1016/j.lithos.2021.106436.

Declaration of Competing Interest

The authors declare that they have no known competing financial interests or personal relationships that could have appeared to influence the work reported in this paper.

References

Alemán-Gallardo, E.A., Ramírez-Fernández, J.A., Weber, B., Velasco-Tapia, F., Casas-Peña, J.M., 2019. Novillo Metamorphic Complex, Huizachal-Peregrina Anticlinorium, Tamaulipas, Mexico: Characterization and development based on whole-rock geochemistry and Nd-isotopic ratios. J. S. Am. Earth Sci. 96, 102382. https://doi.org/10.1016/j.jsames.2019.102382.

Alves, P.V.F.d.S., Botelho, N.F., Dantas, E.L., Cuadros, F.A., 2019. The Cambrian peraluminous Santa Luzia granite suite in the Araguaia Belt, Central Brazil: evidence for closure of the Clymene Ocean based on zircon and monazite U-Pb data. J. S. Am. Earth Sci. 92, 116–133. https://doi.org/10.1016/j.jsames.2019.03.007.

Andersen, T., Elburg, M.A., Magwaza, B.N., . Sources of bias in detrital zircon geochronology: Discordance, concealed lead loss and common lead correction. Earth-Sci. Rev. 197, 102899. https://doi.org/10.1016/j.earscirev.2019.102899.

Aranovich, L.Y., Makhluf, A.R., Manning, C.E., Newton, R.C., 2014. Dehydration melting and the relationship between granites and granulites. Precambrian Res. https://doi.org/10.1016/j.precamres.2014.07.004. Elsevier B.V.

Barbeau, D.L., Olivero, E.B., Swanson-Hysell, N.L., Zahid, K.M., Murray, K.E., Gehrels, G.E., 2009. Detrital-zircon geochronology of the eastern Magallanes foreland basin: implications for Eocene kinematics of the northern Scotia Arc and Drake Passage. Earth Planet. Sci. Lett. 284, 489–503. https://doi.org/10.1016/j.epsl.2009.05.014.

Black, L.P., Kamo, S.L., Allen, C.M., Aleinikoff, J.N., Davis, D.W., Korsch, R.J., Foudoulis, C., 2003. TEMORA 1: a new zircon standard for Phanerozoic U-Pb geochronology. Chem. Geol. 200, 155–170. https://doi.org/10.1016/S0009-2541(03)00165-7.

Blichert-Toft, J., Chauvel, C., Albarède, F., 1997. Separation of Hf and Lu for high-precision isotope analysis of rock samples by magnetic sector-multiple collector ICP-MS. Contrib. Mineral. Petrol. 127, 248–260.

Bouvier, A., Vervoort, J.D., Patchett, P.J., 2008. The Lu-Hf and Sm-Nd isotopic composition of CHUR: Constraints from unequilibrated chondrites and implications for the bulk composition of terrestrial planets. Earth Planet. Sci. Lett. 273, 48–57. https://doi.org/10.1016/j.epsl.2008.06.010.

Boynton, W.V., 1984. Chapter 3 - cosmochemistry of the rare earth elements: meteorite studies. In: Henderson, P. (Ed.), Rare Earth Element Geochemistry, Developments in Geochemistry. Elsevier, pp. 63–114. https://doi.org/10.1016/B978-0-444-42148-7.50008-3.

Burkley, L., 1976. Geochronology of the Central Venezuelan Andes [Ph.D. thesis]. Case Western Reserve University, Cleveland.

Carpentier, M., Chauvel, C., Maury, R.C., Mattielli, N., 2009. The "zircon effect" as recorded by the chemical and Hf isotopic compositions of Lesser Antilles forearc sediments. Earth Planet. Sci. Lett. 287, 86–99. https://doi.org/10.1016/j.epsl.2009.07.043.

Casquet, C., Dahlquist, J.A., Verdecchia, S.O., Baldo, E.G., Galindo, C., Rapela, C.W., Pankhurst, R.J., Morales, M.M., Murra, J.A., Mark Fanning, C., 2018. Review of the Cambrian Pampean orogeny of Argentina; a displaced orogen formerly attached to the Saldania Belt of South Africa? Earth-Science Rev. 177, 209–225. https://doi.org/10.1016/j.earscirev.2017.11.013.

Chauvel, C., Garçon, M., Bureau, S., Besnault, A., Jahn, B.M., Ding, Z., 2014. Constraints from loess on the Hf-Nd isotopic composition of the upper continental crust. Earth Planet. Sci. Lett. 388, 48–58. https://doi.org/10.1016/j.epsl.2013.11.045.

Chen, T., Li, G., Frank, M., Ling, H., 2013. Hafnium isotope fractionation during continental weathering: implications for the generation of the seawater Nd-Hf isotope relationships. Geophys. Res. Lett. 40, 916–920. https://doi.org/10.1002/grl.50217.

Cordani, U.G., Teixeira, W., 2007. Proterozoic accretionary belts in the Amazonian Craton. In: Hatcher Jr., R.D., Carlson, M.P., McBride, J.H., Catalán, J.R.M. (Eds.), 4-D Framework of Continental Crust. Geological Society of America. https://doi.org/10.1130/2007.1200(14).

Coutts, D.S., Matthews, W.A., Hubbard, S.M., 2019. Assessment of widely used methods to derive depositional ages from detrital zircon populations. Geosci. Front. 10, 1421–1435. https://doi.org/10.1016/j.gsf.2018.11.002.

Cullers, R.L., 2002. Implications of elemental concentrations for provenance, redox conditions, and metamorphic studies of shales and limestones near Pueblo, CO, USA. Chem. Geol. 191, 305–327. https://doi.org/10.1016/S0009-2541(02)00133-X.

Dickinson, W.R., Gehrels, G.E., 2009. Use of U-Pb ages of detrital zircons to infer maximum depositional ages of strata: a test against a Colorado Plateau Mesozoic database. Earth Planet. Sci. Lett. 288, 115–125. https://doi.org/10.1016/j.epsl.2009.09.013.

Dostal, J., Keppie, J.D., 2009. Geochemistry of low-grade clastic rocks in the Acatlán Complex of southern Mexico: evidence for local provenance in felsic-intermediate igneous rocks. Sediment. Geol. 222, 241–253. https://doi.org/10.1016/j.sedgeo.2009.09.011.

Dueñas-Jiménez, H., Montalvo-Jónsson, J., 2020. Neoproterozoic records of the Llanos Orientales Basin, Colombia. In: Gómez, J., Mateus-Zabala, D. (Eds.), The Geology of Colombia, Volume 1 Proterozoic – Paleozoic. Servicio Geológico Colombiano, Publicaciones Geológicas Especiales, 35, pp. 91–99. https://doi.org/10.32685/pub.esp.35.2019.05. Bogotá.

Floyd, P.A., Leveridge, B.E., 1987. Tectonic environment of the Devonian Gramscatho basin, south Cornwall: framework mode and geochemical evidence from turbiditic sandstones (England). J. Geol. Soc. 144, 531–542. https://doi.org/10.1144/gsjgs.144.4.0531.

Frei, D., Gerdes, A., 2009. Precise and accurate in situ U-Pb dating of zircon with high sample throughput by automated LA-SF-ICP-MS. Chem. Geol. 261, 261–270. https://doi.org/10.1016/j.chemgeo.2008.07.025.

Galaz, G., Keppie, J.D., Lee, J.K.W., Ortega-Rivera, A., 2013. A high-pressure folded klippe at Tehuitzingo on the western margin of an extrusion zone, Acatlán Complex, southern México. Gondwana Res. 23, 641–660. https://doi.org/10.1016/j.gr.2012.04.011.

Gale, A., Dalton, C.A., Langmuir, C.H., Su, Y., Schilling, J.G., 2013. The mean composition of ocean ridge basalts. Geochem. Geosyst. 14, 489–518. https://doi.org/10.1029/2012GC004334.

Garcia, D., Fonteilles, M., Moutte, J., 1994. Sedimentary Fractionations between Al, Ti, and Zr and the Genesis of Strongly Peraluminous Granites, 102. Univ. Chicago Press, pp. 411–422. https://doi.org/10.1086/629683.

García-Ramírez, C.A., Casadiegos-Agudelo, L., Castellanos-Meléndez, M.P., 2019. Petrology and geochemistry of the Silgara schists in the Silos area, Santander Massif, Colombia. DYNA 86, 271–280. https://doi.org/10.15446/dyna.v86n209.75648.

Gehrels, G., 2014. Detrital zircon U-Pb geochronology applied to tectonics. Annu. Rev. Earth Planet. Sci. 42, 127–149. https://doi.org/10.1146/annurev-earth-050212-124012.

Gehrels, G.E., Valencia, V.A., Ruiz, J., 2008. Enhanced precision, accuracy, efficiency, and spatial resolution of U-Pb ages by laser ablation-multicollector-inductively coupled plasma-mass spectrometry. Geochem. Geophys. Geosyst. 9, 1–13. https://doi.org/10.1029/2007GC001805.

Gerdes, A., Zeh, A., 2006. Combined U-Pb and Hf isotope LA-(MC-)ICP-MS analyses of detrital zircons: comparison with SHRIMP and new constraints for the provenance

and age of an Armorican metasediment in Central Germany. Earth Planet. Sci. Lett. 249, 47–61. https://doi.org/10.1016/j.epsl.2006.06.039.

Gillis, R.J., Gehrels, G.E., Ruiz, J., Flores de Dios, L.A., 2005. Detrital zircon provenance of Cambrian – Ordovician and Carboniferous strata of the Oaxaca terrane, southern Mexico. Sediment. Geol. 182, 87–100. https://doi.org/10.1016/j.sedgeo.2005.07.013.

González de Juana, C., de Arozena, J.M.I., Cadillat, X.P., 1980. Geología de Venezuela y de sus Cuencas Petrolíferas. Ediciones Foninves, Caracas.

González-Guzmán, R., Weber, B., Manjarrez-Juárez, R., Cisneros de León, A., Hecht, L., Herguera-García, J.C., 2016a. Provenance, age constraints and metamorphism of Ediacaran metasedimentary rocks from the El Triunfo Complex (SE Chiapas, México): evidence for Rodinia breakup and Iapetus active margin. Int. Geol. Rev. 58, 2065–2091. https://doi.org/10.1080/00206814.2016.1207208.

González-Guzmán, R., Weber, B., Tazzo-Rangel, M.D., Solari, L., 2016b. Validation of digestion and element separation methods and a new data reduction program (IsotopeHf ®) for Lu-Hf isotope dilution analysis by MC-ICP-MS. Rev. Mex. Ciencias Geol. 33, 254–269.

Grauch, R.I., 1975. Geología de la Sierra Nevada al sur de Mucuchíes, Andes venezolanos: Una región metamórfica de aluminosilicatos. Boletín Geol. del Minist. Minas e Hidrocarburos XII 339–441.

Herron, M.M., 1988. Geochemical Classification of Terrigenous Sands and Shales from Core or Log Data. J. Sediment. Petrol. 58, 820–829. https://doi.org/10.1306/212F8E77-2B24-11D7-8648000102C1865D.

Horton, B.K., Saylor, J.E., Nie, J., Mora, A., Parra, M., Reyes-Harker, A., Stockli, D.F., 2010. Linking sedimentation in the northern Andes to basement configuration, Mesozoic extension, and Cenozoic shortening: evidence from detrital zircon U-Pb ages, Eastern Cordillera, Colombia. Bull. Geol. Soc. Am. 122, 1423–1442. https://doi.org/10.1130/B30118.1.

Ibañez-Mejia, M., 2020. The putumayo orogen of Amazonia: a synthesis. In: Gómez, J., Mateus-Zabala, D. (Eds.), The Geology of Colombia, Volume 1 Proterozoic – Paleozoic, Servicio Geológico Colombiano, Publicaciones Geológicas Especiales, 35, pp. 101–131. https://doi.org/10.32685/pub.esp.35.2019.06. Bogotá.

Ibañez-Mejia, M., Cordani, U.G., 2020. Zircon U–Pb geochronology and Hf–Nd–O isotope geochemistry of the paleo– to Mesoproterozoic basement in the westernmost Guiana Shield. In: Gómez, J., Mateus-Zabala, D. (Eds.), The Geology of Colombia, Volume 1 Proterozoic – Paleozoic, Servicio Geológico Colombiano, Publicaciones Geológicas Especiales, 35, pp. 65–90. https://doi.org/10.32685/pub.esp.35.2019.04. Bogotá.

Jackson, S.E., Pearson, N.J., Griffin, W.L., Belousova, E.A., 2004. The application of laser ablation-inductively coupled plasma-mass spectrometry to in situ U-Pb zircon geochronology. Chem. Geol. 211, 47–69. https://doi.org/10.1016/j.chemgeo.2004.06.017.

Jenchen, U., 2018. Petrography and geochemistry of the Triassic El Tranquilo Group, Deseado Massif, Patagonia, Argentina: implications for provenance and tectonic setting. J. S. Am. Earth Sci. 88, 530–550. https://doi.org/10.1016/j.jsames.2018.09.007.

Keppie, J.D., Dostal, J., Miller, B.V., Ramos-Arias, M.A., Morales-Gámez, M., Nance, R.D., Murphy, J.B., Ortega-Rivera, A., Lee, J.W.K., Housh, T., Cooper, P., 2008. Ordovician-earliest Silurian rift tholeiites in the Acatlán Complex, southern Mexico: evidence of rifting on the southern margin of the Rheic Ocean. Tectonophysics 461, 130–156. https://doi.org/10.1016/j.tecto.2008.01.010.

Klein, E.L., Lopes, E.C.S., Rodrigues, J.B., Souza-Gaia, S.M., Cordani, U.G., 2020. Rhyacian and Neoproterozoic magmatic associations of the Gurupi Belt, Brazil: Implications for the tectonic evolution, and regional correlations. Geosci. Front. 11, 2243–2269. https://doi.org/10.1016/j.gsf.2020.02.016.

Kröner, A., Wan, Y., Liu, X., Liu, D., 2014. Dating of zircon from high-grade rocks: which is the most reliable method? Geosci. Front. 5, 515–523. https://doi.org/10.1016/j.gsf.2014.03.012.

Kroonenberg, S.B., 2019. The proterozoic basement of the Western Guiana Shield and the Northern Andes. In: Cediel, F., Shaw, R.P. (Eds.), Geology and Tectonics of Northwestern South America. Frontiers in Earth Sciences. Springer, pp. 115–189. https://doi.org/10.1007/978-3-319-76132-9_3.

Le Bas, M.J., Le Maitre, R.W., Streckeisen, A., Zanettin, B., 1986. A chemical classification of volcanic rocks based on the total alkali-silica diagram. J. Petrol. 27, 745–750. https://doi.org/10.1093/petrology/27.3.745.

Liew, T.C., Hofmann, A.W., 1988. Precambrian crustal components, plutonic associations, plate environment of the Hercynian Fold Belt of Central Europe: indications from a Nd and Sr isotopic study. Contrib. Mineral. Petrol. 98, 129–138. https://doi.org/10.1007/BF00402106.

Lugmair, G.W., Marti, K., 1978. Lunar initial 143Nd/144Nd: Differential evolution of the lunar crust and mantle. Earth Planet. Sci. Lett. 39, 349–357.

Lyubetskaya, T., Korenaga, J., 2007. Chemical composition of Earth's primitive mantle and its variance: 1. Method and results. J. Geophys. Res. Solid Earth 112, 1–21. https://doi.org/10.1029/2005JB004223.

Mantilla-Figueroa, L.C., García-Ramírez, C.A., Valencia, V.A., 2016a. Nuevas evidencias que soportan la escisión de la formación Silgará y propuesta de un nuevo marco estratigráfico para el basamento metamórfico del Macizo de Santander (Cordillera Oriental de Colombia). Rev. la Acad. Colomb. Ciencias Exactas, Físicas y Nat. 40, 320. https://doi.org/10.18257/raccefyn.303.

Mantilla-Figueroa, L.C., García-Ramírez, C.A., Valencia, V.A., 2016b. Propuesta de escisión de la denominada "Formación Silgará" (Macizo de Santander, Colombia), a partir de edades U-Pb en circones detríticos. Bol. Geol. 38, 33–50. https://doi.org/10.18273/revbol.v38n1-2016002.

Martens, U., Weber, B., Valencia, V.A., 2010. U/Pb geochronology of Devonian and older Paleozoic beds in the southeastern Maya Block, Central America: its affinity with peri-Gondwanan terranes. Bull. Geol. Soc. Am. 122, 815–829. https://doi.org/10.1130/B26405.1.

Mason, C.C., Romans, B.W., Stockli, D.F., Mapes, R.W., Fildani, A., 2019. Detrital zircons reveal sea-level and hydroclimate controls on Amazon River to deep-sea fan sediment transfer. Geology 47, 563–567. https://doi.org/10.1130/G45852.1.

McLennan, S.M., Hemming, S., McDaniel, D.K., Hanson, G.N., 1993. Geochemical approaches to sedimentation, provenance and tectonics: processes controlling the composition of clastic sediments. Spec. Pap. Geol. Soc. Am. 284, 21–40.

Mejía-Arango, M.I., Garcia-Zapata, G., Martens, U., 2012. Caracterización petrográfica, geoquímica y edad de la sienita nefelínica de san josé del guaviare. Boletín Geol. 34, 15–26.

Merdith, A.S., Williams, S.E., Collins, A.S., Tetley, M.G., Mulder, J.A., Blades, M.L., Young, A., Armistead, S.E., Cannon, J., Zahirovic, S., Müller, R.D., 2021. Extending full-plate tectonic models into deep time: linking the Neoproterozoic and the Phanerozoic. Earth-Sci. Rev. 214, 103477. https://doi.org/10.1016/j.earscirev.2020.103477.

Morales-Gámez, M., Keppie, J.D., Norman, M., 2008. Ordovician-Silurian rift-passive margin on the Mexican margin of the Rheic Ocean overlain by Carboniferous-Permian periarc rocks: evidence from the eastern Acatlán Complex, southern Mexico. Tectonophysics 461, 291–310. https://doi.org/10.1016/j.tecto.2008.01.014.

Müller, R.D., Cannon, J., Qin, X., Watson, R.J., Gurnis, M., Williams, S., Pfaffelmoser, T., Seton, M., Russell, S.H.J., Zahirovic, S., 2018. GPlates: building a virtual earth through deep time. Geochem. Geophys. Geosyst. 19, 2243–2261. https://doi.org/10.1029/2018GC007584.

Murphy, J.B., Keppie, J.D., Nance, R.D., Miller, B.V., Dostal, J., Middleton, M., Fernández-Suárez, J., Jeffries, T.E., Storey, C.D., 2006. Geochemistry and U–Pb protolith ages of eclogitic rocks of the Asís Lithodeme, Piaxtla Suite, Acatlán complex, southern Mexico: tectonothermal activity along the southern margin of the Rheic Ocean. J. Geol. Soc. Lond. 163, 683–695. https://doi.org/10.1144/0016-764905-108.

Nasdala, L., Corfu, F., Valley, J.W., Spicuzza, M.J., Wu, F.Y., Li, Q.L., Yang, Y.H., Fisher, C., Münker, C., Kennedy, A.K., Reiners, P.W., Kronz, A., Wiedenbeck, M., Wirth, R., Chanmuang, C., Zeug, M., Váczi, T., Norberg, N., Häger, T., Kröner, A., Hofmeister, W., 2016. Zircon M127 – a homogeneous reference material for SIMS U–Pb geochronology combined with hafnium, oxygen and, potentially, Lithium Isotope Analysis. Geostand. Geoanalytical Res. 40, 457–475. https://doi.org/10.1111/ggr.12123.

Nebel, O., Vroon, P.Z., van Westrenen, W., Iizuka, T., Davies, G.R., 2011. The effect of sediment recycling in subduction zones on the Hf isotope character of new arc crust, Banda arc, Indonesia. Earth Planet. Sci. Lett. 303, 240–250. https://doi.org/10.1016/j.epsl.2010.12.053.

Nesbitt, H.W., Young, G.M., 1984. Prediction of some weathering trends of plutonic and volcanic rocks based on thermodynamic and kinetic considerations. Geochim. Cosmochim. Acta 48, 1523–1534. https://doi.org/10.1016/0016-7037(84)90408-3.

Oliveira, E.P., Bueno, J.F., Mcnaughton, N.J., Filho, A.F., Nascimiento, R.S., Donatti-Filho, J.P., 2015. Age, composition, and source of continental arc- and syn-collision granites of the Neoproterozoic Sergipano Belt, Southern Borborema. J. S. Am. Earth Sci. 58, 257–280.

Oriolo, S., Schulz, B., Geuna, S., González, P.D., Otamendi, J.E., Sláma, J., Druguet, E., Siegesmund, S., 2021. Early Paleozoic accretionary orogens along the Western Gondwana margin. Geosci. Front. 12, 109–130. https://doi.org/10.1016/j.gsf.2020.07.001.

Ortega-Gutiérrez, F., Elías-Herrera, M., Morán-Zenteno, D.J., Solari, L., Weber, B., Luna-González, L., 2018. The pre-Mesozoic metamorphic basement of Mexico, 1.5 billion years of crustal evolution. Earth-Sci. Rev. 183, 2–37. https://doi.org/10.1016/j.earscirev.2018.03.006.

Ortega-Obregón, C., Duncan Keppie, J., Brendan Murphy, J., Lee, J.K.W., Ortega-Rivera, A., 2009. Geology and geochronology of Paleozoic rocks in western Acatlán complex, southern Mexico: evidence for contiguity across an extruded high-pressure belt and constraints on Paleozoic reconstructions. Bull. Geol. Soc. Am. 121, 1678–1694. https://doi.org/10.1130/B26597.1.

Ortega-Obregon, C., Murphy, J.B., Keppie, J.D., 2010. Geochemistry and Sm-Nd isotopic systematics of Ediacaran-Ordovician, sedimentary and bimodal igneous rocks in the western Acatlán complex, southern Mexico: evidence for rifting on the southern margin of the Rheic Ocean. Lithos 114, 155–167. https://doi.org/10.1016/j.lithos.2009.08.005.

Ostos, M., Yoris, F., Lallemant, H.G.A., 2005. Overview of the southeast Caribbean–South American plate boundary zone. In: Lallemant, H.G.A., Sisson, V.B. (Eds.), Special Paper 394: Caribbean-South American Plate Interactions, Venezuela, pp. 53–89.

Palheta, E., Matos de Abreu, F., Moura, C., 2009. Granitóides proterozóicos como marcadores da evolução geotectônica da região nordeste do Pará, Brasil. Rev. Bras. Geociências 39, 647–657. https://doi.org/10.25249/0375-7536.2009394647657.

Patchett, P.J., Ruiz, J., 1987. Nd isotopic ages of crust formation and metamorphism in the Precambrian of eastern and southern Mexico. Contrib. Mineral. Petrol. 96, 523–528. https://doi.org/10.1007/BF01166697.

Pearce, J.A., 1983. Role of the sub-continental lithosphere in magma genesis at active continental margins. In: Hawkesworth, C.J., Norry, M.J. (Eds.), Continental Basalts and Mantle Xenoliths. Shiva Publications, Nantwich, pp. 230–249.

Pearce, J.A., 1996. A User's Guide to Basalt Discriminant Diagrams. In: Wyman, D.A. (Ed.), In Trace Element Geochemistry of Volcanic Rocks: Applications for Massive Sulphide Exploration, 12. Geological Association of Canada Short Course Notes, pp. 79–113.

Pimentel, M.M., 2016. The tectonic evolution of the Neoproterozoic Brasília Belt, Central Brazil: a geochronological and isotopic approach. Brazilian J. Geol. 46, 67–82. https://doi.org/10.1590/2317-4889201620150004.

Pollock, J.C., Hibbard, J.P., Sylvester, P.J., 2009. Early Ordovician rifting of Avalonia and birth of the Rheic Ocean: U-Pb detrital zircon constraints from Newfoundland. J. Geol. Soc. Lond. 166, 501–515. https://doi.org/10.1144/0016-76492008-088.

Ramos, V.A., 2018. The Famatinian orogen along the protomargin of Western Gondwana: evidence for a nearly continuous Ordovician magmatic arc between Venezuela and Argentina Victor. In: Folguera, A., Contreras Reyes, E., Heredia, N., Encinas, A., Iannelli, S.B., Oliveros, V., Arriagada, C. (Eds.), The Evolution of the Chilean-Argentinean Andes. Springer, pp. 154–183. https://doi.org/10.1007/978-3-319-67774-3.

Ramos-Arias, M.A., Keppie, J.D., 2011. U–Pb Neoproterozoic–Ordovician protolith age constraints for high- to medium-pressure rocks thrust over low-grade metamorphic rocks in the Ixcamilpa area, Acatlán Complex, southern Mexico. Can. J. Earth Sci. 48, 45–61. https://doi.org/10.1139/E10-082.

Reimink, J.R., Davies, J.H.F.L., Waldron, J.W.F., Rojas, X., 2016. Dealing with discordance: a novel approach for analysing U–Pb detrital zircon datasets. J. Geol. Soc. Lond. 173, 577–585. https://doi.org/10.1144/jgs2015-114.

Restrepo, J.J., Martens, U., Giraldo-Ramírez, W., 2020. The Anacona Terrane: a small early Paleozoic peri–Gondwanan terrane in the Cauca–Romeral fault system. In: Gómez, J., Mateus-Zabala, D. (Eds.), The Geology of Colombia, Volume 1 Proterozoic – Paleozoic, Servicio Geológico Colombiano, Publicaciones Geológicas Especiales, 35, pp. 37–63. https://doi.org/10.32685/pub.esp.35.2019.03. Bogotá.

Restrepo-Pace, P.A., Ruiz, J., Gehrels, G.E., Cosca, M., 1997. Geochronology and Nd isotopic data of Grenville-age rocks in the Colombian Andes: new constraints for late Proterozoic-early Paleozoic paleocontinental reconstructions of the Americas. Earth Planet. Sci. Lett. 150, 427–441.

Ross, P.S., Bédard, J.H., 2009. Magmatic affinity of modern and ancient subalkaline volcanic rocks determined from trace-element discriminant diagrams. Can. J. Earth Sci. 46, 823–839. https://doi.org/10.1139/E09-054.

Rubatto, D., 2017. Zircon: the metamorphic mineral. Rev. Mineral. Geochem. 83, 261–295. https://doi.org/10.2138/rmg.2017.83.9.

Rudnick, R.L., Gao, S., 2013. Composition of the Continental Crust, 2nd ed. Elsevier Ltd. https://doi.org/10.1016/B978-0-08-095975-7.00301-6 Treatise on Geochemistry: Second Edition.

Ruiz, J., Patchett, P.J., Ortega-Gutierrez, F., 1988. Proterozoic and Phanerozoic basement terranes of Mexico from Nd isotopic studies. Bull. Geol. Soc. Am. 100, 274–281. https://doi.org/10.1130/0016-7606(1988)100<0274:PAPBTO>2.3.CO;2.

Sawyer, E.W., 2008. Atlas of Migmatites. The Canadian Mineralogist Special Publication 9. Canadian Science Publishing, Ottawa. https://doi.org/10.1139/9780660197876.

Scherer, E., Münker, C., Mezger, K., 2001. Calibration of the lutetium-hafnium clock. Science (80-.) 293, 683–687. https://doi.org/10.1126/science.1061372.

Schmitt, R. Da S., Fragoso, R.D.A., Collins, A.S., Siegesmund, S., 2018. In: Basei, M.A.S., Oyhantçabal, P., Oriolo, S. (Eds.), Suturing Gondwana in the Cambrian: the orogenic events of the final amalgamation. Springer International Publishing, Geology of Southwest Gondwana, pp. 411–432. https://doi.org/10.1007/978-3-319-68920-3.

Scotese, C.R., 2016. PaleoAtlas for GPlates and the PaleoData Plotter Program, PALEOMAP Project [WWW Document]. URL https://www.earthbyte.org/paleomap-paleoatlas-for-gplates/.

Sisson, V.B., Avé Lallement, H.G., Ostos, M., Blythe, A.E., Snee, L.W., Copeland, P., Wright, J.E., Donelick, R.A., Guth, L.R., 2005. Overview of radiometric ages in three allochthonous belts of Northern Venezuela: old ones, new ones, and their impact on regional geology. In: Avé Lallement, H.G., Sisson, V.B. (Eds.), Caribbean–South American Plate Interactions, Venezuela. Geological Society of America Special Paper, 394, pp. 91–117. https://doi.org/10.1130/0-8137-2394-9.91.

Sláma, J., Košler, J., Condon, D.J., Crowley, J.L., Gerdes, A., Hanchar, J.M., Horstwood, M.S.A., Morris, G.A., Nasdala, L., Norberg, N., Schaltegger, U., Schoene, B., Tubrett, M.N., Whitehouse, M.J., 2008. Plešovice zircon - a new natural reference material for U-Pb and Hf isotopic microanalysis. Chem. Geol. 249, 1–35. https://doi.org/10.1016/j.chemgeo.2007.11.005.

Söderlund, U., Patchett, P.J., Vervoort, J.D., Isachsen, C.E., 2004. The176Lu decay constant determined by Lu-Hf and U-Pb isotope systematics of Precambrian mafic intrusions. Earth Planet. Sci. Lett. 219, 311–324. https://doi.org/10.1016/S0012-821X(04)00012-3.

Solari, L.A., Ortega-Gutiérrez, F., Elías-Herrera, M., Schaaf, P., Norman, M., de león, R.T., Ortega-Obregón, C., Chiquín, M., Ical, S.M., 2009. U-Pb zircon geochronology of Palaeozoic units in Western and Central Guatemala: insights into the tectonic evolution of Middle America. Geol. Soc. London Spec. Publ. 328, 295–313. https://doi.org/10.1144/SP328.12.

Spencer, C.J., 2020. Continuous continental growth as constrained by the sedimentary record. Am. J. Sci. 320, 373–401. https://doi.org/10.2475/04.2020.02.

Spencer, C.J., Kirkland, C.L., Taylor, R.J.M., 2016. Strategies towards statistically robust interpretations of in situ U-Pb zircon geochronology. Geosci. Front. 7, 581–589. https://doi.org/10.1016/j.gsf.2015.11.006.

Suhr, N., Rojas-Agramonte, Y., Chew, D.M., Pinto, A.J., Villagómez-Díaz, D., Toulkeridis, T., Mertz-Kraus, R., 2019. Detrital-zircon geochronology and provenance of the El Oro Metamorphic Complex, ecuador: geodynamic implications for the evolution of the western Gondwana margin. J. S. Am. Earth Sci. 90, 520–539. https://doi.org/10.1016/j.jsames.2018.12.010.

Suttner, L.J., Dutta, P.K., 1986. Alluvial sandstone composition and paleoclimate, I. Framework mineralogy. J. Sediment. Petrol. 56, 329–345. https://doi.org/10.1306/212F8909-2B24-11D7-8648000102C1865D.

Talavera-Mendoza, O., Ruiz, J., Gehrels, G.E., Meza-Figueroa, D.M., Vega-Granillo, R., Campa-Uranga, M.F., 2005. U-Pb geochronology of the Acatlán Complex and implications for the Paleozoic paleogeography and tectonic evolution of southern Mexico. Earth Planet. Sci. Lett. 235, 682–699. https://doi.org/10.1016/j.epsl.2005.04.013.

Taylor, S.R., McLennan, S.M., 1985. The Continental Crust; its Composition and Evolution; an Examination of the Geochemical Record Preserved in Sedimentary Rocks. Blackwell Scientific, Oxford.

Tazzo-Rangel, M.D., Weber, B., González-Guzmán, R., Valencia, V.A., Frei, D., Schaaf, P., Solari, L.A., 2019. Multiple metamorphic events in the Palaeozoic Mérida Andes basement, Venezuela: insights from U–Pb geochronology and Hf–Nd isotope systematics. Int. Geol. Rev. 61, 1557–1593. https://doi.org/10.1080/00206814.2018.1522520.

Tazzo-Rangel, M.D., Weber, B., Schmitt, A.K., González-Guzmán, R., Cisneros de León, A., Hecht, L., 2020. Permo–Triassic metamorphism in the Mérida Andes, Venezuela: new insights from geochronology, O-isotopes, and geothermobarometry. Int. J. Earth Sci. https://doi.org/10.1007/s00531-020-01926-5. Springer, Berlin, Heidelberg.

Teixeira, W., Geraldes, M.C., Matos, R., Ruiz, A.S., Saes, G., Vargas-Matto, G., 2010. A review of the tectonic evolution of the Sunsás belt, SW Amazonian Craton. J. S. Am. Earth Sci. 29, 47–60. https://doi.org/10.1016/j.jsames.2009.09.007.

Thiry, M., 2000. Palaeoclimatic interpretation of clay minerals in marine deposits: an outlook from the continental origin. Earth Sci. Rev. 49, 201–221. https://doi.org/10.1016/S0012-8252(99)00054-9.

Torres de León, R., Solari, L.A., Ortega-Gutiérrez, F., Martens, U., 2012. The Chortís Block-southwestern México connections: U-Pb zircon geochronology constraints. Am. J. Sci. 312, 288–313. https://doi.org/10.2475/03.2012.02.

Torsvik, T., Cocks, L., 2016. Cambrian. In: Earth History and Palaeogeography. Cambridge University Press, Cambridge, pp. 85–100. https://doi.org/10.1017/9781316225523.006.

van der Lelij, R., Spikings, R., Ulianov, A., Chiaradia, M., Mora, A., 2016. Palaeozoic to Early Jurassic history of the northwestern corner of Gondwana, and implications for the evolution of the Iapetus, Rheic and Pacific Oceans. Gondwana Res. 31, 271–294. https://doi.org/10.1016/j.gr.2015.01.011.

Vega-Granillo, R., Talavera-Mendoza, O., Meza-Figueroa, D., Ruiz, J., Gehrels, G.E., López-Martínez, M., de la Cruz-Vargas, J.C., 2007. Pressure-temperature-time evolution of Paleozoic high-pressure rocks of the Acatlán Complex (southern Mexico): implications for the evolution of the Iapetus and Rheic Oceans. Bull. Geol. Soc. Am. 119, 1249–1264. https://doi.org/10.1130/B226031.1.

Vermeesch, P., 2007. Quantitative geomorphology of the White Mountains (California) using detrital apatite fission track thermochronology. J. Geophys. Res. Earth Surf. 112, 1–11. https://doi.org/10.1029/2006JF000671.

Vermeesch, P., 2013. Multi-sample comparison of detrital age distributions. Chem. Geol. 341, 140–146. https://doi.org/10.1016/j.chemgeo.2013.01.010.

Vermeesch, P., 2018. IsoplotR: a free and open toolbox for geochronology. Geosci. Front. 9, 1479–1493. https://doi.org/10.1016/j.gsf.2018.04.001.

Vervoort, J.D., Patchett, P.J., Albarède, F., Blichert-Toft, J., Rudnick, R., Downes, H., 2000. Hf-Nd isotopic evolution of the lower crust. Earth Planet. Sci. Lett. 181, 115–129. https://doi.org/10.1016/S0012-821X(00)00170-9.

Vervoort, J.D., Plank, T., Prytulak, J., 2011. The Hf-Nd isotopic composition of marine sediments. Geochim. Cosmochim. Acta 75, 5903–5926. https://doi.org/10.1016/j.gca.2011.07.046.

Vinagre, R., Trouw, R.A.J., Mendes, J.C., Duffles, P., Peternel, R., Matos, G., 2014. New evidence of a magmatic arc in the southern Brasília Belt, Brazil: the Serra da Água Limpa batholith (Socorro-Guaxupé Nappe). J. S. Am. Earth Sci. 54, 120–139. https://doi.org/10.1016/j.jsames.2014.05.002.

Viscarret, P., Wright, J., Urbani, F., 2009. New U-Pb zircon ages of El Baúl Massif, Cojedes State, Venezuela. Rev. Tec. la Fac. Ing. Univ. del Zulia 32, 210–221.

Weber, B., Köhler, H., 1999. Sm–Nd, Rb–Sr and U–Pb geochronology of a Grenville Terrane in Southern Mexico: origin and geologic history of the Guichicovi Complex. Precambrian Res. 96, 245–262. https://doi.org/10.1016/S0301-9268(99)00012-1.

Weber, B., Scherer, E.E., Martens, U.K., Mezger, K., 2012. Where did the lower Paleozoic rocks of Yucatan come from? A U-Pb, Lu-Hf, and Sm-Nd isotope study. Chem. Geol. 312–313, 1–17. https://doi.org/10.1016/j.chemgeo.2012.04.010.

Weber, B., González-Guzmán, R., Manjarrez-Juárez, R., Cisneros de León, A., Martens, U., Solari, L., Hecht, L., Valencia, V., 2018. Late Mesoproterozoic to Early Paleozoic history of metamorphic basement from the southeastern Chiapas Massif Complex, Mexico, and implications for the evolution of NW Gondwana. Lithos 300–301, 177–199. https://doi.org/10.1016/j.lithos.2017.12.009.

Whitney, D.L., Evans, B.W., 2010. Abbreviations for names of rock-forming minerals. Am. Mineral. 95, 185–187. https://doi.org/10.2138/am.2010.3371.

Wiedenbeck, M., Aleé, P., Corfu, F., Griffin, W.L., Meier, M., Oberli, F., Von Quadt, A., Roddick, J.C., Spiegel, W., 1995. Three Natural Zircon Standards for U-Th-Pb, Lu-Hf, Trace Element and Ree Analyses. Geostand. Newslett. 19, 1–23. https://doi.org/10.1111/j.1751-908X.1995.tb00147.x.

Williams, I.S., 2001. Response of detrital and zircon and monazite, and their U-Pb isotopic systems, to regional metamorphism and host-rock partial melting, Cooma Complex, Southeastern Australia. Aust. J. Earth Sci. 48, 557–580. https://doi.org/10.1046/j.1440-0952.2001.00883.x.

Wimmenauer, W., 1984. Das Prävariskische Kristallin im Schwarzwald. Fortschritte der Mineral. 62, 69–86.

Young, G.M., 2018. Chapter 2 - precambrian glacial deposits: their origin, tectonic setting, and key role in earth evolution. In: Menzies, J., van der Meer, J.J.M. (Eds.), Past Glacial Environments, Second edition. Elsevier, pp. 17–45. https://doi.org/10.1016/B978-0-08-100524-8.00001-4.

Zimmermann, S., Mark, C., Chew, D., Voice, P.J., 2018. Maximising data and precision from detrital zircon U-Pb analysis by LA-ICPMS: the use of core-rim ages and the single-analysis concordia age. Sediment. Geol. 375, 5–13. https://doi.org/10.1016/j.sedgeo.2017.12.020.